J. Fluid Mech. (2008), vol. 601, pp. 199–227. © 2008 Cambridge University Press
doi:10.1017/S0022112008000463 Printed in the United Kingdom

How rapidly oscillating collapsible tubes extract energy from a viscous mean flow

MATTHIAS HEIL[1] AND SARAH L. WATERS[2]†
[1]School of Mathematics, University of Manchester, Oxford Road, Manchester M13 9PL, UK
[2]Division of Applied Mathematics, School of Mathematical Sciences,
University of Nottingham, University Park, Nottingham, NG7 2RD, UK

(Received 21 August 2007 and in revised form 8 January 2008)

We present a combined theoretical and computational analysis of three-dimensional unsteady finite-Reynolds-number flows in collapsible tubes whose walls perform prescribed high-frequency oscillations which resemble those typically observed in experiments with a Starling resistor. Following an analysis of the flow fields, we investigate the system's overall energy budget and establish the critical Reynolds number, Re_{crit}, at which the wall begins to extract energy from the flow. We conjecture that Re_{crit} corresponds to the Reynolds number beyond which collapsible tubes are capable of performing sustained self-excited oscillations. Our computations suggest a simple functional relationship between Re_{crit} and the system parameters, and we present a scaling argument to explain this observation. Finally, we demonstrate that, within the framework of the instability mechanism analysed here, self-excited oscillations of collapsible tubes are much more likely to develop from steady-state configurations in which the tube is buckled non-axisymmetrically, rather than from axisymmetric steady states, which is in agreement with experimental observations.

1. Introduction

Fluid–structure interaction plays an important role in many physiological systems that convey fluid within elastic (collapsible) vessels. For instance, pulse wave propagation in the arteries is possible only because the arterial walls are elastic; expiratory flow limitation is known to be caused by the flow-induced collapse of the pulmonary airways; wheezing during forced expiration and the development of Korotkoff sounds during sphygmomanometry are believed to be manifestations of self-excited oscillations of the vessel walls, generated by their interaction with the fluid flow.

Most experimental studies of flow in collapsible tubes are performed with the Starling resistor, consisting of a thin-walled elastic tube, mounted on two rigid tubes (figure 1). Flow is driven through the system either by an applied pressure drop, or by a volumetric pump located at the far upstream or downstream ends of the rigid tubes. The elastic tube is contained in a pressure chamber which makes it possible to control the external pressure, p_{ext}, independently of the fluid pressure. As long as the external pressure is sufficiently small (or negative) relative to the fluid pressure, the collapsible tube deforms axisymmetrically; in this mode, large changes in fluid

---

† Present address: Oxford Centre for Industrial and Applied Mathematics, Mathematical Institute, 24–29 St Giles', Oxford, OX1 3LB, UK.

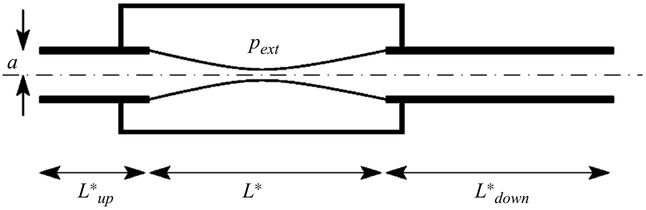

FIGURE 1. Sketch of the Starling resistor, a thin-walled elastic tube, mounted on two rigid tubes and enclosed in a pressure chamber.

pressure are required to change the tube shape. When the external pressure exceeds a certain critical value, the tube tends to buckle non-axisymmetrically; in this mode the tube is very flexible so that even small changes in fluid pressure can lead to large changes in the tube shape, resulting in strong fluid–structure interaction and complicated pressure-drop/flow relationships see (e.g. Bertram, Raymond & Pedley 1990; Bertram & Castles 1999). Arguably the most intriguing feature of the Starling resistor is that the system readily develops large-amplitude self-excited oscillations of great complexity (Bertram *et al.* 1990). Experiments by Bertram & Tscherry (2006) show that self-excited oscillations can develop at modest Reynolds numbers (of the order of a few hundred), and that they develop primarily from steady-state configurations in which the collapsible tube is in a non-axisymmetrically buckled state (Bertram, personal communication 2007).

Despite continued interest in the problem since the late 1960s (comprehensively reviewed in Heil & Jensen 2003), there is still no rational theoretical model that explains the mechanism(s) responsible for the onset of self-excited oscillations in three-dimensional finite-length collapsible tubes. In fact, to date it is not even clear if the self-excited oscillations observed in the experiments arise primarily through a fluid-mechanical instability (possibly slightly modified by the presence of the elastic walls), or if the oscillations develop through a genuine interaction between fluid and solid mechanics. Furthermore, different instability mechanisms may operate in different regions of parameter space. For instance, some of the very-high-frequency small-amplitude oscillations observed in some of Bertram's experiments may simply represent a passive response of the tube wall to the highly unsteady turbulent flow within, whereas turbulence cannot be responsible for the oscillations observed in Bertram & Tscherry's (2006) experiments at moderate Reynolds numbers.

In early one-dimensional models of flow in collapsible tubes, the wall deformation was described by a so-called 'tube law', an assumed functional relationship between the tube's cross-sectional area, A^*, and the local transmural (internal minus external) pressure, p_{tm}. Writing the tube law as $p_{tm} = \mathfrak{P}(A^*)$, the wave speed c of small-amplitude perturbations travelling along the tube is given by

$$c^2 = \frac{A^*}{\rho_f} \frac{\partial \mathfrak{P}(A^*)}{\partial A^*}, \tag{1.1}$$

where ρ_f is the fluid density. Within the framework of the one-dimensional theory, the development of self-excited oscillations has occasionally been linked to the onset of flow-limitation, which is predicted to occur when the fluid velocity approaches the wave speed c anywhere along the tube. However, subsequent studies, such as the experiments by Bertram & Raymond (1991) or the computations by Luo & Pedley (2000) have cast doubt over a causal link between these two phenomena.

Jensen & Heil (2003) developed a rational theoretical model that explains the onset of self-excited oscillations in finite-length parallel-walled channels in which part of one wall is replaced by a pre-stressed elastic membrane – a two-dimensional equivalent of the Starling resistor. Focusing on a particular region of parameter space (high Reynolds number and large wall tension), they identified an instability mechanism that causes the development of high-frequency self-excited oscillations. Asymptotic methods were employed to derive explicit predictions for the frequencies and the growth (or decay) rates of the oscillation as a function of the Reynolds number, and thus the critical Reynolds number for the onset of self-excited oscillations was established. The asymptotic predictions were confirmed by direct numerical simulations which showed that the mechanism responsible for the initial instability also controls the large-amplitude oscillations that develop subsequently. Briefly, Jensen & Heil (2003) showed that high-frequency wall oscillations generate an unsteady inviscid core flow in which fluid that is displaced by the transversely oscillating wall performs axial sloshing motions. Thin Stokes layers form on the channel walls. A key ingredient of the instability mechanism is that the oscillatory core flow can create a net influx of (kinetic) energy into the system. The development of self-excited oscillations depends crucially on the ratio of this influx of energy to the viscous dissipation in the Stokes layers.

Motivated by Jensen & Heil's (2003) study, Heil & Waters (2006) subsequently investigated how (and whether) the two-dimensional instability mechanism can be adjusted to explain the experimentally observed instabilities in three-dimensions. They found that, while the main ingredients of the instability mechanism are independent of the spatial dimension, there are some important differences between the two-dimensional and three-dimensional systems. In particular, slight buckling of a cylindrical tube about its axisymmetric configuration causes only very small changes in its volume. Therefore, at small amplitudes, the oscillatory wall deformation induces only very small net axial flows – the dominant oscillatory flows occur in the tube's transverse cross-sections. This is an important difference to the behaviour in the two-dimensional system and suggests that in three-dimensions, Jensen & Heil's instability mechanism will operate efficiently only if the tube oscillates about a non-axisymmetrically buckled mean configuration and/or if the amplitude of the oscillations reaches a certain critical magnitude. Heil & Waters (2006) assumed that the oscillatory axial *velocities* could be neglected and employed a combination of numerical and asymptotic techniques to study the two-dimensional flows that develop in the transverse cross-sections of an oscillating elastic tube. Their study identified the physical mechanisms that control the dynamics of these oscillations and provided explicit predictions for their period and decay rate. (In their two-dimensional model, the transverse flows do not interact with the steady through flow and can therefore not extract any energy from it – the oscillations therefore invariably decay.)

In this paper, we extend the previous analyses to three dimensions and focus on the transfer of energy between the fluid and the solid, exploiting the fact that in the fluid–structure interaction problem, oscillations will grow in amplitude if and only if the wall extracts energy from the flow. Our approach is as follows. We assume that the wall performs a time-periodic oscillation about a time-mean configuration, and prescribe the wall displacement field and the period of the oscillation. We aim to identify regions of parameter space in which a net influx of kinetic energy over the in- and outflow boundaries provides a sufficient source of energy that the wall can extract energy from the flow. To guide our exploration of parameter space, we note that the instantaneous flux of kinetic energy over the far-upstream or far-downstream

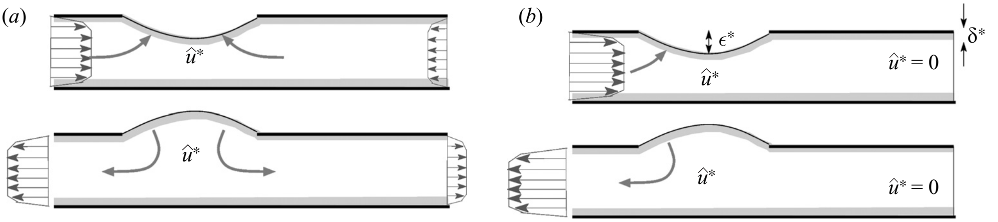

FIGURE 2. (*a*) Sketch of the sloshing flows generated by the oscillatory wall motion of amplitude ϵ^* in the two-dimensional collapsible channel analysed by Jensen & Heil (2003). The sloshing flow has an inviscid core region, with Stokes layers of thickness δ^* near the walls. (*b*) The influx of kinetic energy is maximized if the sloshing flows are suppressed at the far downstream end of the system. In both cases the mean flow (not shown) is assumed to be from left to right.

ends of the system is given by

$$\mathscr{F}^{[kin]*} = \int \boldsymbol{u}^* \cdot \boldsymbol{n} \, \left(\tfrac{1}{2}\,\rho_f\,(\boldsymbol{u}^*)^2\right) \mathrm{d}A^*, \tag{1.2}$$

where $\boldsymbol{u}^*$ is the velocity field, ρ_f the fluid density, and $\boldsymbol{n}$ the outer unit normal on the in- or outflow cross-section, A^*. Assuming that the flow is fully developed at the in- and outflow cross-sections and that it can be decomposed into a steady mean component, $\overline{\boldsymbol{u}}^*$, and a time-periodic perturbation with zero mean, $\widehat{\boldsymbol{u}}^*$, which is dominated by a single Fourier mode, the net influx of kinetic energy over one period of the oscillation, $\overline{\mathscr{F}^{[kin]*}}$, is given by

$$\overline{\mathscr{F}^{[kin]*}} \approx 3 \int \overline{\boldsymbol{u}}^* \cdot \boldsymbol{n} \, \left(\tfrac{1}{2}\,\rho_f\,\overline{\left(\widehat{\boldsymbol{u}}^*\right)^2}\right) \mathrm{d}A^*, \tag{1.3}$$

where the overbar denotes the time-average over one period of the oscillation. Hence, we have a net influx of kinetic energy if the time-averaged square of the velocity perturbations, $\overline{(\widehat{\boldsymbol{u}}^*)^2}$, at the inflow exceeds that at the outflow. Jensen & Heil (2003) showed that, for pressure-driven flows, this is likely to occur if the length of the downstream rigid tube exceeds that of its upstream counterpart (figure 2*a*). The net influx of kinetic energy is maximized if the fluctuations at the downstream end are suppressed so that $\widehat{\boldsymbol{u}}^* \equiv \boldsymbol{0}$ (figure 2*b*). Experimentally, this could be achieved by controlling the flow rate using a volumetric pump located at the far downstream end of the system. In that case, the entire volume of fluid that is displaced by the wall motion contributes to the velocity fluctuations at the far upstream end where it generates a net influx of kinetic energy, while no kinetic energy fluctuations are lost through the downstream end. Equation (1.3) also shows that the net influx of kinetic energy can be increased by two independent mechanisms: (i) by increasing the magnitude of the sloshing flows, e.g. via an increase in the amplitude of the wall motion; or (ii) by increasing the mean flow since this increases the advection of kinetic energy into the domain.

2. The model

We consider the unsteady finite-Reynolds-number flow of a viscous fluid (density ρ_f and viscosity μ) through a collapsible tube of undeformed radius a and length L^*, mounted on two rigid tubes of lengths L^*_{up} and L^*_{down}, respectively (figure 1). The total length of the tube is $L^*_{total} = L^*_{up} + L^* + L^*_{down}$. (Throughout this paper, asterisks are used to distinguish dimensional quantities from their non-dimensional equivalents.) We assume that the collapsible wall segment performs prescribed time-periodic non-axisymmetric oscillations of period T, either about its undeformed axisymmetric shape or about a non-axisymmetrically buckled configuration. Since the influx of kinetic energy is maximized when the velocity fluctuations at the outflow are suppressed, we control the flow rate at the far downstream end of the system by imposing steady Poiseuille flow with average velocity U at the end of the downstream rigid tube. (For all the cases considered in this study, the length of the downstream rigid tube was sufficiently large for the flow to be fully developed well before reaching the outflow cross-section.) At the inlet, we impose parallel inflow and subject the flow to zero axial traction. In the absence of any wall deformation, the flow is therefore a steady Poiseuille flow.

We scale all lengths on the tube radius, a, time on the period of the oscillation, $t^* = T\,t$, the velocities on the associated unsteady velocity scale, a/T, and all stresses, tractions and the fluid pressure on the associated viscous scale, so that, e.g., $p^* = p\,\mu(a/T)/a = p\,\mu/T$.

We parameterize the non-dimensional position vector to the undeformed wall shape by two Lagrangian coordinates ξ^α $(\alpha = 1, 2)$ as

$$\boldsymbol{r}_w = \left(\cos(\xi^2), \sin(\xi^2), \xi^1\right)^T, \tag{2.1}$$

written here with respect to a Cartesian coordinate system (x, y, z), where $\xi^1 \in [0, L_{total}]$ and $\xi^2 \in [0, 2\pi]$. The wall motion results in the displacement of material particles from their original positions, $\boldsymbol{r}_w(\xi^1, \xi^2)$, to new positions, $\boldsymbol{R}_w(\xi^1, \xi^2, t)$. We denote the amplitude of the wall displacement by $\epsilon^* = a\epsilon$. In the first instance we decompose the displacement field into a (spatial) mode shape, $\boldsymbol{m}(\xi^1, \xi^2)$, and a time-dependent amplitude, $f(t)$, by setting $\boldsymbol{R}_w = \widetilde{\boldsymbol{R}_w}$, where

$$\widetilde{\boldsymbol{R}_w}(\xi^1, \xi^2, t) = \boldsymbol{r}_w(\xi^1, \xi^2) + \epsilon f(t)\,\boldsymbol{m}(\xi^1, \xi^2). \tag{2.2}$$

When analysing the flow field for a specific wall displacement field, we shall use the mode shape

$$\boldsymbol{m}(\xi^1, \xi^2) = \begin{pmatrix} \mathscr{U}(\xi^1)\cos(N\xi^2)\cos(\xi^2) - \mathscr{V}(\xi^1)\sin(N\xi^2)\sin(\xi^2) \\ \mathscr{U}(\xi^1)\cos(N\xi^2)\sin(\xi^2) + \mathscr{V}(\xi^1)\sin(N\xi^2)\cos(\xi^2) \\ \mathscr{W}(\xi^1)\cos(N\xi^2) \end{pmatrix}, \tag{2.3}$$

where $\mathscr{U}(\xi^1) = \mathscr{V}(\xi^1) = \mathscr{W}(\xi^1) = 0$ for $\xi^1 < L_{up}$ and $\xi^1 > L_{up} + L$. This mode shape resembles the eigenmode of a cylindrical shell oscillating in its Nth azimuthal mode (see e.g. Soedel 1993) which is appropriate for small-amplitude oscillations. However, the wall shapes described by (2.3) become increasingly unrealistic as the amplitude of the oscillation is increased. This is because at finite-amplitude, the mode shape (2.3) leads to significant azimuthal stretching of the tube wall, whereas thin-walled elastic shells tend to deform in a mode that minimizes their extensional deformation. Therefore we modified the above wall displacement such that the perimeter of the tube's cross-sections is kept constant. This was achieved by setting

$$\boldsymbol{R}_w(\xi^1, \xi^2, t) = \widetilde{R^z_w}(\xi^1, \xi^2, t)\;\boldsymbol{e}_z + \widetilde{\boldsymbol{R}^\perp_w}(\xi^1, \xi^2, t)\;\mathscr{S}(t, \xi^1; \epsilon), \tag{2.4}$$

where $\widetilde{R^z_w}(\xi^1, \xi^2, t) = \widetilde{\boldsymbol{R}_w}(\xi^1, \xi^2, t) \cdot \boldsymbol{e}_z$ and $\widetilde{\boldsymbol{R}^\perp_w}(\xi^1, \xi^2, t) = \widetilde{\boldsymbol{R}_w}(\xi^1, \xi^2, t) - \widetilde{R^z_w}(\xi^1, \xi^2, t)\,\boldsymbol{e}_z$. The scaling factor $\mathscr{S}(t, \xi^1; \epsilon) = 1 + O(\epsilon^2)$ in (2.4) was chosen such that the tube's cross-sections deform without any net azimuthal stretching; see Appendix A for details.

We assume that the wall displacement field contains a steady and a time-periodic unsteady component so that

$$f(t) = \mathscr{E} + \sin(\Omega t), \tag{2.5}$$

where $\mathscr{E}$ indicates the magnitude of the tube's mean deflection, relative to the amplitude of its oscillations about this mean configuration. If $\mathscr{E} = 0$, the wall performs oscillations about its undeformed axisymmetric shape. The parameter Ω is introduced to facilitate the transfer of our results to the fully coupled fluid–structure interaction problem, where it is important to distinguish between the time scale T used in the non-dimensionalization of the equations, and the actual (and *a priori* unknown) period $\mathscr{T}^* = T\mathscr{T}$ of the coupled oscillations. We define

$$\Omega = 2\pi \frac{T}{\mathscr{T}^*} = 2\pi \frac{1}{\mathscr{T}}, \tag{2.6}$$

and note that for the prescribed wall motions considered in this paper, $\Omega \equiv 2\pi$.

The flow is governed by the non-dimensional Navier–Stokes equations

$$\alpha^2 \left(\frac{\partial \boldsymbol{u}}{\partial t} + \boldsymbol{u} \cdot \nabla \boldsymbol{u} \right) = -\nabla p + \nabla^2 \boldsymbol{u}, \qquad \nabla \cdot \boldsymbol{u} = 0, \tag{2.7}$$

where the Womersley number

$$\alpha^2 = \frac{\rho_f a^2}{\mu T}, \tag{2.8}$$

represents the ratio of unsteady fluid inertia to the viscous forces. The flow is subject to the no-slip conditions

$$\boldsymbol{u} = \frac{\partial \boldsymbol{R}_w}{\partial t} \quad \text{on the wall.} \tag{2.9}$$

The assumption of parallel, axially traction-free inflow implies

$$p = 0, \quad \boldsymbol{u} \cdot \boldsymbol{e}_r = 0, \quad \boldsymbol{u} \cdot \boldsymbol{e}_\theta = 0 \quad \text{at } z = 0, \tag{2.10}$$

where $\boldsymbol{e}_r$, $\boldsymbol{e}_\theta$ and $\boldsymbol{e}_z$ are the unit coordinate vectors in a cylindrical polar coordinate system (r, θ, z). At the outflow we prescribe a Poiseuille profile,

$$\boldsymbol{u} = \frac{2}{St} \left(1 - r^2\right) \boldsymbol{e}_z \quad \text{at } z = L_{total}, \tag{2.11}$$

where the Strouhal number

$$St = \frac{a}{UT}, \tag{2.12}$$

represents the ratio of the time scales for the mean axial flow to the period of the wall oscillation. We note that the ratio of Womersley and Strouhal numbers is the Reynolds number associated with the steady flow

$$\frac{\alpha^2}{St} = \frac{\rho_f a U}{\mu} = Re. \tag{2.13}$$

The problem is thus governed by three main dimensionless parameters: the Womersley number, α^2, the Strouhal number, St, and the amplitude of the wall displacement field ϵ. We note that the inverse Strouhal number provides a measure of the mean flow through the tube.

When analysing the system's energy budget we will frequently refer to the energy equation which, in terms of the non-dimensional variables, is given by

$$\underbrace{\alpha^2 \frac{\mathrm{d}}{\mathrm{d}t}\int_V \left(\tfrac{1}{2}\,\boldsymbol{u}^2\right)\mathrm{d}V}_{\mathrm{d}\Pi_{kin}/\mathrm{d}t} - \underbrace{\alpha^2\int_{inflow} \boldsymbol{e}_z\cdot\boldsymbol{u}\left(\tfrac{1}{2}\,\boldsymbol{u}^2\right)\mathrm{d}A}_{\mathscr{F}^{[kin]}_{in}} + \underbrace{\alpha^2\int_{outflow} \boldsymbol{e}_z\cdot\boldsymbol{u}\left(\tfrac{1}{2}\,\boldsymbol{u}^2\right)\mathrm{d}A}_{\mathscr{F}^{[kin]}_{out}}$$

$$= \underbrace{\int_{inflow} \boldsymbol{t}\cdot\boldsymbol{u}\,\mathrm{d}A}_{\mathscr{P}_{in}} + \underbrace{\int_{outflow} \boldsymbol{t}\cdot\boldsymbol{u}\,\mathrm{d}A}_{\mathscr{P}_{out}} + \underbrace{\int_{wall} \boldsymbol{t}\cdot\boldsymbol{u}\,\mathrm{d}A}_{\mathscr{P}_{wall}} - \underbrace{\int_V \Phi\,\mathrm{d}V}_{\mathscr{D}}, \qquad (2.14)$$

where $\boldsymbol{t}$ is the traction that acts on the fluid at the relevant surfaces. The various integrals represent the rate of change of kinetic energy, the flux of kinetic energy over the inflow and outflow cross-sections, the rate-of-work done on the fluid by the applied traction at the inflow, outflow, and by the wall, respectively, and the viscous dissipation, expressed as the integral of $\Phi = 2\boldsymbol{E}:\boldsymbol{E}$, where $\boldsymbol{E} = (1/2)(\nabla\boldsymbol{u} + (\nabla\boldsymbol{u})^T)$ is the rate-of-strain tensor.

3. Scaling and asymptotic analysis

Before discussing the numerical solution of the problem, we first employ asymptotic methods to analyse the flow field in a particular parameter regime, exploiting the fact that, for high-frequency wall oscillations, the Womersley and Strouhal numbers are likely to be large. In addition, we initially restrict attention to small wall deflections so that $\epsilon \ll 1$.

3.1. *Scaling*

In the absence of any wall deformation, the flow is steady Poiseuille flow. We therefore decompose the velocity field into a Poiseuille profile and add steady and unsteady (with zero mean) perturbations that are generated by the wall motion and mean deformation. Scaling the former on the mean velocity, U, and the latter two on the wall velocity, $\epsilon\, a/T$, respectively, yields

$$\boldsymbol{u} = \frac{1}{St}\boldsymbol{U} + \epsilon(\overline{\boldsymbol{u}} + \widehat{\boldsymbol{u}}), \qquad (3.1)$$

where

$$\boldsymbol{U} = 2(1 - r^2)\boldsymbol{e}_z = \overline{W}(r)\,\boldsymbol{e}_z. \qquad (3.2)$$

Throughout this paper we use overbars to denote time-mean quantities and hats to denote unsteady quantities with zero mean. Similarly, we separate the pressure into a Poiseuille contribution, P, which we scale on the viscous pressure scale, $\mu U/a$, and add steady and unsteady (with zero mean) perturbations. Since the pressure perturbations are induced by the high-frequency wall motion, we expect them to be dominated by inertial effects and scale them on $\epsilon\,\rho_f\, a^2/T^2$. Thus, we write the pressure as

$$p = \frac{1}{St}\,P + \epsilon\,\alpha^2(\overline{p} + \widehat{p}), \qquad (3.3)$$

where $P = -8z$. We substitute (3.1) and (3.3) into (2.7) and decompose the equations into their unsteady (with zero mean) components,

$$\frac{\partial\widehat{\boldsymbol{u}}}{\partial t} + \left(\frac{1}{St}\boldsymbol{U} + \epsilon\overline{\boldsymbol{u}}\right)\cdot\nabla\widehat{\boldsymbol{u}} + \widehat{\boldsymbol{u}}\cdot\nabla\left(\frac{1}{St}\boldsymbol{U} + \epsilon\overline{\boldsymbol{u}}\right) + \epsilon\widehat{\widehat{\boldsymbol{u}}\cdot\nabla\widehat{\boldsymbol{u}}} = -\nabla\widehat{p} + \frac{1}{\alpha^2}\nabla^2\widehat{\boldsymbol{u}}, \qquad (3.4)$$

$$\nabla \cdot \widehat{\boldsymbol{u}} = 0, \tag{3.5}$$

and their time-average over one period of the oscillation,

$$\epsilon \overline{\boldsymbol{u}} \cdot \nabla \overline{\boldsymbol{u}} + \epsilon \overline{\widehat{\boldsymbol{u}} \cdot \nabla \widehat{\boldsymbol{u}}} + \frac{1}{St}(\overline{\boldsymbol{u}} \cdot \nabla \boldsymbol{U} + \boldsymbol{U} \cdot \nabla \overline{\boldsymbol{u}}) = -\nabla \overline{p} + \frac{1}{\alpha^2} \nabla^2 \overline{\boldsymbol{u}}, \quad \nabla \cdot \overline{\boldsymbol{u}} = 0. \tag{3.6}$$

In these expressions, the overbar and hat operators extract the time-average and time-periodic (with zero mean) components from their arguments.

From (2.9), the boundary condition at the tube wall is

$$\frac{1}{St} \boldsymbol{U} + \epsilon (\widehat{\boldsymbol{u}} + \overline{\boldsymbol{u}}) = \frac{\partial \boldsymbol{R}_w}{\partial t}, \tag{3.7}$$

and from (2.10) and (2.11) we have

$$\overline{p} = \widehat{p} = 0, \ \overline{\boldsymbol{u}} \cdot \boldsymbol{e}_r = \widehat{\boldsymbol{u}} \cdot \boldsymbol{e}_r = 0, \ \overline{\boldsymbol{u}} \cdot \boldsymbol{e}_\theta = \widehat{\boldsymbol{u}} \cdot \boldsymbol{e}_\theta = 0 \ \text{ at } \ z = 0, \tag{3.8}$$

$$\overline{\boldsymbol{u}} = \widehat{\boldsymbol{u}} = \boldsymbol{0} \ \text{ at } \ z = L_{total}. \tag{3.9}$$

3.2. *The parameter regime for the asymptotic analysis*

We now analyse the above equations in a particular parameter regime. We assume that the wall deflection is small, corresponding to $\epsilon \ll 1$ and $\mathscr{E} = O(1)$. Furthermore, we assume that the period of the wall oscillation is much shorter than the typical time scale for the mean flow so that $St^{-1} \ll 1$. This suggests an expansion of all quantities in powers of ϵ and St^{-1}, i.e.

$$\widehat{\boldsymbol{u}} = \widehat{\boldsymbol{u}}_0 + O(\epsilon, St^{-1}), \qquad \widehat{p} = \widehat{p}_0 + O(\epsilon, St^{-1}), \tag{3.10}$$

where $(\widehat{\boldsymbol{u}}_0, \widehat{p}_0)$ are the leading-order contributions to $(\widehat{\boldsymbol{u}}, \widehat{p})$; similar expansions are employed for the remaining dependent variables. High-frequency wall oscillations are characterized by large Womersley numbers, $\alpha^2 \gg 1$, and we assume that

$$\epsilon, \frac{1}{St} \ll \frac{1}{\alpha} \ll 1. \tag{3.11}$$

This corresponds to a regime in which the thickness of the Stokes layers that develop on the oscillating tube walls is much larger than the wall deflection. The relative size of the terms in the constraint (3.11) determines the Reynolds number of the mean flow. Small-Reynolds-number flows are characterized by $1/St \ll 1/\alpha^2 \ll 1$ whereas large Reynolds numbers require $1/\alpha^2 \ll 1/St \ll 1$.

Inserting the expansions (3.10) into (3.4), (3.5), we find that the leading-order unsteady flow $(\widehat{\boldsymbol{u}}_0, \widehat{p}_0)$ is governed by

$$\frac{\partial \widehat{\boldsymbol{u}}_0}{\partial t} = -\nabla \widehat{p}_0 + \frac{1}{\alpha^2} \nabla^2 \widehat{\boldsymbol{u}}_0, \quad \nabla \cdot \widehat{\boldsymbol{u}}_0 = 0, \tag{3.12}$$

subject to

$$\widehat{\boldsymbol{u}}_0|_{r=1} = \Omega(\cos(N\theta)\mathscr{U}(z)\,\boldsymbol{e}_r + \sin(N\theta)\mathscr{V}(z)\,\boldsymbol{e}_\theta + \cos(N\theta)\mathscr{W}(z)\,\boldsymbol{e}_z)\mathrm{e}^{\mathrm{i}\Omega t} \ \text{ at } \ r = 1, \tag{3.13}$$

where the real part is understood, and the same boundary conditions (3.8) and (3.9) that we imposed on $\widehat{\boldsymbol{u}}$ and $\widehat{p}$.

Our assumption that $1/\alpha \ll 1$ implies that in the core region, away from the tube walls, the viscous terms in (3.12) can be neglected so that the flow is governed by the inviscid equations

$$\partial \widehat{\boldsymbol{u}}_0 / \partial t = -\nabla \widehat{p}_0. \tag{3.14}$$

Since inviscid flows cannot satisfy the tangential components of the no-slip condition (3.13), we expect the development of Stokes (boundary) layers of thickness $\delta \propto \alpha^{-1}$ on the tube walls. Within these layers the viscous terms have a size of $O(1)$, justifying their retention in (3.12).

We are now in a position to estimate the size of $\overline{\boldsymbol{u}}$ and $\overline{p}$. Referring to (3.6), we see that the contributions to $\overline{\boldsymbol{u}}$ and $\overline{p}$ arise from the nonlinear inertia terms, and the deformation of the wall shape (through the boundary conditions). The leading-order correction to the steady flow, $(\overline{\boldsymbol{u}}_0, \overline{p}_0)$, is governed by

$$-\nabla\overline{p}_0 + \frac{1}{\alpha^2}\nabla^2\overline{\boldsymbol{u}}_0 = \boldsymbol{0}, \quad \nabla\cdot\overline{\boldsymbol{u}}_0 = 0 \tag{3.15}$$

subject to $\overline{\boldsymbol{u}}_0|_{r=1} = \boldsymbol{0}$, and the same boundary conditions (3.8) and (3.9) that we imposed on $\overline{\boldsymbol{u}}$ and $\overline{p}$. A consistent solution is $\overline{\boldsymbol{u}}_0 = \boldsymbol{0}$, $\overline{p}_0 = 0$, indicating that the wall motion only induces small changes $(O(\epsilon^2, \epsilon/St))$ to the steady flow.

3.3. *Analysis of the leading-order unsteady perturbation*

To solve the leading-order unsteady flow equations, (3.12), subject to (3.13), we consider the Fourier expansion of $\mathscr{U}(z)$,

$$\mathscr{U}(z) = \sum_{m=0}^{\infty}\left(U_m^{[c]}\cos(\lambda_m z) + U_m^{[s]}\sin(\lambda_m z)\right), \tag{3.16}$$

where $\lambda_m = m\pi/L_{total}$, with similar expansions for $\mathscr{V}$ and $\mathscr{W}$. The displacement of the tube wall is zero at $z=0$ and $z = L_{total}$ and thus we must have $U_m^{[c]} = V_m^{[c]} = W_m^{[c]} = 0$.

We seek asymptotic solutions for the flow quantities. Following Heil & Waters (2006), we expand the dependent variables in powers of α^{-1} as follows:

$$\widehat{\boldsymbol{u}}_0 = \left(\widehat{\boldsymbol{u}}_{00} + \frac{1}{\alpha}\widehat{\boldsymbol{u}}_{01} + \cdots\right)\mathrm{e}^{\mathrm{i}\Omega t}, \quad \widehat{p}_0 = \left(\widehat{p}_{00} + \frac{1}{\alpha}\widehat{p}_{01} + \cdots\right)\mathrm{e}^{\mathrm{i}\Omega t}, \tag{3.17a,b}$$

where the real part is understood here and in the analysis that follows. Since we expect the development of a Stokes (boundary) layer of thickness $\delta = O(\alpha^{-1})$ near the wall, we introduce the boundary-layer coordinate $n = \alpha(1-r)$, and expand the variables in the boundary layer as

$$\widehat{u}_0 = \left(\widehat{U}_w + \frac{1}{\alpha}\widehat{U}_{00} + \frac{1}{\alpha^2}\widehat{U}_{01} + \cdots\right)\mathrm{e}^{\mathrm{i}\Omega t}, \tag{3.18}$$

$$\widehat{v}_0 = \left(\widehat{V}_{00} + \frac{1}{\alpha}\widehat{V}_{01} + \frac{1}{\alpha^2}\widehat{V}_{02} + \cdots\right)\mathrm{e}^{\mathrm{i}\Omega t}, \tag{3.19}$$

$$\widehat{w}_0 = \left(\widehat{W}_{00} + \frac{1}{\alpha}\widehat{W}_{01} + \frac{1}{\alpha^2}\widehat{W}_{02} + \cdots\right)\mathrm{e}^{\mathrm{i}\Omega t}, \tag{3.20}$$

$$\widehat{p}_0 = \left(\widehat{P}_{00} + \frac{1}{\alpha}\widehat{P}_{01} + \frac{1}{\alpha^2}\widehat{P}_{02} + \cdots\right)\mathrm{e}^{\mathrm{i}\Omega t}, \tag{3.21}$$

where

$$\widehat{U}_w = \Omega\cos(N\theta)\,\mathscr{U}(z). \tag{3.22}$$

The core flow solutions are matched to those in the boundary layer via Van Dyke's matching rule (Van Dyke 1964).

3.3.1. *The leading-order in α^{-1} problem*

Substitution of (3.17*a*,*b*) into (3.12) shows that the leading-order problem for $(\widehat{\boldsymbol{u}}_{00}, \widehat{p}_{00})$ is

$$\mathrm{i}\Omega\widehat{\boldsymbol{u}}_{00} = -\nabla\widehat{p}_{00}, \qquad \nabla\cdot\widehat{\boldsymbol{u}}_{00} = 0. \tag{3.23}$$

These equations must be solved subject to the matching condition whose leading-order contribution requires that $\widehat{u}_{00} = \widehat{U}_w$ at $r = 1$. Applying $\nabla\cdot$ to (3.23) gives $\nabla^2\widehat{p}_{00} = 0$ which is then solved subject to $\partial\widehat{p}_{00}/\partial r = -\mathrm{i}\Omega^2\mathscr{U}(z)\cos(N\theta)$ at $r = 1$. We consider a separable solution for $\widehat{p}_{00}$ of the form

$$\widehat{p}_{00} = \mathrm{i}\Omega\cos(N\theta)\sum_{m=1}^{\infty} A_m I_N(\lambda_m r)\sin(\lambda_m z), \tag{3.24}$$

where I_N is the modified Bessel function of order N. From the boundary conditions at $r = 1$ we have $A_m = -\Omega U_m^{[s]}/(\lambda_m I_N'(\lambda_m))$. The core velocities are then determined using (3.23), so that

$$\widehat{u}_{00} = -\cos(N\theta)\sum_{m=1}^{\infty} A_m\lambda_m I_N'(\lambda_m r)\sin(\lambda_m z), \quad \text{etc.} \tag{3.25}$$

As expected, the velocity field does not satisfy the no-slip condition that requires $\widehat{v}_{00} = \widehat{w}_{00} = 0$ at $r = 1$, and it is necessary to consider flow in the Stokes layer. The leading-order equations that govern this flow are

$$\frac{\partial\widehat{P}_{00}}{\partial n} = 0, \quad \mathrm{i}\Omega\widehat{V}_{00} = -\frac{\partial\widehat{P}_{00}}{\partial\theta} + \frac{\partial^2\widehat{V}_{00}}{\partial n^2}, \quad \mathrm{i}\Omega\widehat{W}_{00} = -\frac{\partial\widehat{P}_{00}}{\partial z} + \frac{\partial^2\widehat{W}_{00}}{\partial n^2}, \tag{3.26}$$

$$-\frac{\partial\widehat{U}_{00}}{\partial n} + \widehat{U}_w + \frac{\partial\widehat{V}_{00}}{\partial\theta} + \frac{\partial\widehat{W}_{00}}{\partial z} = 0, \tag{3.27}$$

which must be solved subject to the no-slip boundary conditions $\widehat{U}_{00} = 0$, $\widehat{V}_{00} = \widehat{V}_w = \Omega\sin(N\theta)\mathscr{V}$ and $\widehat{W}_{00} = \widehat{W}_w = \Omega\cos(N\theta)\mathscr{W}$ at $n = 0$. The matching conditions as $n \to \infty$ are $\lim_{n\to\infty}\widehat{V}_{00} = \widehat{v}_{00}|_1$, with similar expressions for $\widehat{W}_{00}$ and $\widehat{P}_{00}$. The solution is

$$\begin{aligned}\widehat{U}_{00} = {} & -\cos(N\theta)\sum_{m=1}^{\infty}\lambda_m I_N'(\lambda_m)(B_m\sin(\lambda_m z) + C_m\cos(\lambda_m z))(1 - \mathscr{F}(n)) \\ & + A_m(\lambda_m I_N'(\lambda_m) - (N^2 + \lambda_m^2)I_N(\lambda_m))n\sin(\lambda_m z),\end{aligned} \tag{3.28}$$

$$\widehat{V}_{00} = \sin(N\theta)\sum_{m=1}^{\infty}(\Omega V_m^{[s]}\mathscr{F}(n) + A_m N I_N(\lambda_m)(1 - \mathscr{F}(n)))\sin(\lambda_m z), \tag{3.29}$$

$$\widehat{W}_{00} = \cos(N\theta)\sum_{m=1}^{\infty}\Omega W_m^{[s]}\mathscr{F}(n)\sin(\lambda_m z) - A_m\lambda_m I_N(\lambda_m)(1 - \mathscr{F}(n))\cos(\lambda_m z), \tag{3.30}$$

$$\widehat{P}_{00} = \mathrm{i}\Omega\cos(N\theta)\sum_{m=1}^{\infty} A_m I_N(\lambda_m)\sin(\lambda_m z), \tag{3.31}$$

where $\mathscr{F}(n) = \exp(-(1+\mathrm{i})\sqrt{\Omega/2}n)$ and

$$B_m = -\frac{(1-\mathrm{i})}{\sqrt{2\Omega}\lambda_m I_N'(\lambda_m)}\left(N\Omega V_m^{[s]} - A_m\left(\lambda_m^2 + N^2\right)I_N(\lambda_m)\right), \quad C_m = -\frac{\sqrt{\Omega}(1-i)}{\sqrt{2}I_N'(\lambda_m)}W_m^{[s]}. \tag{3.32}$$

3.3.2. *The first-order in α^{-1} problem*

The governing equations for $\widehat{\boldsymbol{u}}_{01}$, $\widehat{p}_{01}$ are

$$\mathrm{i}\Omega\widehat{\boldsymbol{u}}_{01} = -\nabla\widehat{p}_{01}, \qquad \nabla\cdot\widehat{\boldsymbol{u}}_{01} = 0, \tag{3.33a,b}$$

which, from the matching condition must be solved subject to

$$\widehat{u}_{01}|_1 = -\sum_{m=1}^{\infty}\lambda_m I_N'(\lambda_m)\,(B_m\sin(\lambda_m z) + C_m\cos(\lambda_m z))\cos(N\theta). \tag{3.34}$$

The solution is

$$\widehat{p}_{01} = \mathrm{i}\Omega\cos(N\theta)\sum_{m=1}^{\infty}(B_m\sin(\lambda_m z) + C_m\cos(\lambda_m z))\,I_N(\lambda_m r), \tag{3.35}$$

with the core velocities determined using (3.33a), so that

$$\widehat{u}_{01} = -\cos(N\theta)\sum_{m=1}^{\infty}\lambda_m(B_m\sin(\lambda_m z) + C_m\cos(\lambda_m z))I_N'(\lambda_m r), \quad \text{etc.} \tag{3.36}$$

Again, these solutions do not satisfy the no-slip condition which requires $\widehat{v}_{01} = \widehat{w}_{01} = 0$ at $r = 1$. Thus it is again necessary to consider flow in the Stokes layer. The equations which govern this flow are

$$\mathrm{i}\Omega\widehat{V}_{01} = -\frac{\partial\widehat{P}_{01}}{\partial\theta} - n\frac{\partial\widehat{P}_{00}}{\partial\theta} + \frac{\partial^2\widehat{V}_{01}}{\partial n^2} - \frac{\partial\widehat{V}_{00}}{\partial n}, \tag{3.37}$$

$$\frac{\partial\widehat{P}_{01}}{\partial n} = \mathrm{i}\Omega\widehat{U}_w, \tag{3.38}$$

$$\mathrm{i}\Omega\widehat{W}_{01} = -\frac{\partial\widehat{P}_{01}}{\partial z} + \frac{\partial^2\widehat{W}_{01}}{\partial n^2} - \frac{\partial\widehat{W}_{00}}{\partial n}, \tag{3.39}$$

$$-\frac{\partial\widehat{U}_{01}}{\partial n} + n\widehat{U}_w + \widehat{U}_{00} + n\frac{\partial\widehat{V}_{00}}{\partial\theta} + \frac{\partial\widehat{V}_{01}}{\partial\theta} + \frac{\partial\widehat{W}_{01}}{\partial z} = 0, \tag{3.40}$$

which must satisfy the no-slip condition $\widehat{V}_{01} = \widehat{W}_{01} = 0$ at $n = 0$ and the matching conditions $\lim_{n\to\infty}\widehat{V}_{01} = -n(\partial\widehat{v}_{00}/\partial r)|_1 + \widehat{v}_{01}|_1$, with similar expressions for $\widehat{W}_{01}$ and $\widehat{P}_{01}$.

The solution is

$$\begin{aligned}\widehat{V}_{01} &= \sin(N\theta)\sum_{m=1}^{\infty}NI_N(\lambda_m)(B_m\sin(\lambda_m z) + C_m\cos(\lambda_m z))(1 - \mathscr{F}(n)) + n\sin(\lambda_m z)\\ &\qquad\times\left(A_m N(I_N(\lambda_m z) - \lambda_m I_N'(\lambda_m)) + \tfrac{1}{2}\left(\Omega V_m^{[s]} - A_m N I_N(\lambda_m)\right)\mathscr{F}(n)\right),\end{aligned} \tag{3.41}$$

$$\begin{aligned}\widehat{W}_{01} &= \cos(N\theta)\sum_{m=1}^{\infty}\lambda_m I_N(\lambda_m)(-B_m\cos(\lambda_m z) + C_m\sin(\lambda_m z))(1 - \mathscr{F}(n)))\\ &\qquad + n\lambda_m A_m\left(\lambda_m I_N'(\lambda_m) + \frac{I_N(\lambda_m)}{2}\mathscr{F}(n)\right)\cos(\lambda_m z) + \frac{n\Omega W_m^{[s]}}{2}\mathscr{F}(n)\sin(\lambda_m z),\end{aligned} \tag{3.42}$$

$$\begin{aligned}\widehat{P}_{01} &= \mathrm{i}\Omega\cos(N\theta)\sum_{m=1}^{\infty}I_N(\lambda_m)(B_m\sin(\lambda_m z) + C_m\cos(\lambda_m z))\\ &\qquad - nA_m\lambda_m I_N'(\lambda_m)\sin(\lambda_m z).\end{aligned} \tag{3.43}$$

The radial velocity component, $\widehat{U}_{01}$, can be obtained from (3.40), but is not required for the first two terms of the expansion (3.17*a*).

3.3.3. *The composite solution*

To facilitate direct comparison with the numerical solution, we construct composite expansions that are valid throughout the entire domain. Using standard procedures (see e.g. Hinch 1991) the expansions for velocity and pressure given in (3.24), (3.25), (3.28), (3.29), (3.30), (3.31), (3.35), (3.36), (3.41), (3.42) and (3.43) can be combined to the composite approximations

$$\begin{aligned}\widehat{p}_0 &= \mathrm{i}\Omega\cos(N\theta)\mathrm{e}^{\mathrm{i}\Omega t}\sum_{m=1}^{\infty}\\ &\quad\times\left(A_m\sin(\lambda_m z)+\frac{1}{\alpha}(B_m\sin(\lambda_m z)+C_m\cos(\lambda_m z))\right)I_N(\lambda_m r), \qquad (3.44)\end{aligned}$$

$$\begin{aligned}\widehat{u}_0 &= -\cos(N\theta)\mathrm{e}^{\mathrm{i}\Omega t}\sum_{m=1}^{\infty}A_m\lambda_m I_N'(\lambda_m r)\sin(\lambda_m z)\\ &\quad+\frac{\lambda_m}{\alpha}(B_m\sin(\lambda_m z)+C_m\cos(\lambda_m z))(I_N'(\lambda_m r)-I_N'(\lambda_m)\mathscr{G}(r)), \qquad (3.45)\end{aligned}$$

$$\begin{aligned}\widehat{v}_0 &= N\sin(N\theta)\mathrm{e}^{\mathrm{i}\Omega t}\sum_{m=1}^{\infty}\left(A_m\mathscr{I}(r)+\frac{\Omega V_m^{[s]}}{N}\mathscr{H}(r)\right)\sin(\lambda_m z)\\ &\quad+\frac{1}{\alpha}(B_m\sin(\lambda_m z)+C_m\cos(\lambda_m z))\left(\frac{I_N(\lambda_m r)}{r}-I_N(\lambda_m)\mathscr{G}(r)\right), \qquad (3.46)\end{aligned}$$

$$\begin{aligned}\widehat{w}_0 &= -\cos(N\theta)\mathrm{e}^{\mathrm{i}\Omega t}\sum_{m=1}^{\infty}(A_m\lambda_m(I_N(\lambda_m r)-I_N(\lambda_m)\mathscr{H}(r))-\Omega W_m^{[s]}\mathscr{H}(r))\sin(\lambda_m z)\\ &\quad+\frac{\lambda_m}{\alpha}(B_m\cos(\lambda_m z)-C_m\sin(\lambda_m z))(I_N(\lambda_m r)-I_N(\lambda_m)\mathscr{G}(r)), \qquad (3.47)\end{aligned}$$

where $\mathscr{G}(r)=\mathscr{F}(\alpha(1-r))$, $\mathscr{H}(r)=\mathscr{G}(r)(1+(1-r)/2)$ and $\mathscr{I}(r)=I_N(\lambda_m r)/r-I_N(\lambda_m)\mathscr{H}(r)$. Plots of these velocity and pressure fields will be shown in § 4.1.

4. Numerical simulations

For finite-amplitude wall oscillations, the governing equations must be solved numerically. We performed direct numerical simulations using Heil & Hazel's (2006) object-oriented multi-physics finite-element library oomph-lib. In experiments, collapsible tubes tend to buckle in a two-lobed mode, and therefore we restricted the computations to wall motions with an azimuthal wavenumber of $N=2$ and discretized only a quarter of the domain, $x, y \geqslant 0$. Symmetry conditions were applied in the planes $x=0$ and $y=0$. The arbitrary Lagrangian–Eulerian form of the Navier–Stokes equations was discretized with hexahedral Taylor–Hood (Q2Q1) elements on a body-fitted mesh in which the node-update in response to the wall deformation was performed by oomph-lib's MacroElement representation of the domain. The mesh was carefully designed to achieve a higher element density near the tube walls where we expect the development of thin Stokes layers. The time-integration was performed with a fourth-order BDF scheme with constant time step, using the asymptotic solution derived in § 3.2 as the initial condition. The time-integration covered at least five periods of the oscillation to ensure that the system had settled into a time-periodic state. The large system of nonlinear algebraic equations to be solved at every time step of the implicit time-integration procedure was solved by oomph-lib's Newton solver. BiCGStab, preconditioned by Elman, Silvester & Wathen (2005) least-squares-commutator Navier–Stokes preconditioner, was used to solve the linear systems arising in the course of the Newton iteration. The standard spatial resolution involved approximately 52 600 degrees of freedom and time-stepping was performed with 160 time steps per period of the oscillation. Selected runs were repeated with higher spatial and temporal resolutions to confirm the mesh- and time-step-independence of the results; see Appendix B.

To perform the numerical simulations, we imposed the radial displacement field

$$\mathscr{U}(\xi^1) = \begin{cases} 0 & \text{for } \xi^1 < L_{up}, \\ \dfrac{1}{2}\left(1 - \cos\left(\dfrac{2\pi(\xi^1 - L_{up})}{L}\right)\right) & \text{for } L_{up} < \xi^1 < L_{up} + L, \\ 0 & \text{for } \xi^1 > L + L_{up}, \end{cases} \tag{4.1}$$

for which the Fourier coefficients in (3.16) are given by

$$U_m^{[s]} = \frac{4L_{total}^2}{\pi m(m^2L^2 - 4L_{total}^2)}\left(\cos(\lambda_m(L_{up} + L)) - \cos(\lambda_m L_{up})\right). \tag{4.2}$$

We used the same mode shape for the azimuthal displacement field by setting $\mathscr{V}(\xi^1) = \mathbb{A}\,\mathscr{U}(\xi^1)$, where $\mathbb{A}$ is the amplitude ratio of the azimuthal and radial wall displacements. In most computations (apart from those presented in § 5.4), we suppressed the axial wall displacements by setting $\mathscr{W}(\xi^1) = 0$. All simulations were performed with $\mathbb{A} = -1/2$. With this choice, the deformation of the tube's cross-sections resembles that of thin-walled elastic rings oscillating *in vacuo*. The tube lengths were set to be $L_{up} = 1$ and $L = L_{down} = 5$.

4.1. *Small-amplitude oscillations*

Figure 3 illustrates the three-dimensional flow in the oscillating tube at four equally spaced instants during one period of the oscillation, for a small-amplitude wall motion ($\epsilon = 10^{-3}$) with a ratio of mean-to-oscillatory deflection of $\mathscr{E} = 1$, a mean flow of $St^{-1} = 10^{-3}$, and a Womersley number of $\alpha^2 = 50$. In each case, the upper figure shows the axial velocity profiles in the tube's cross-sections while the lower figure shows the profiles of the axial velocity perturbation, obtained by subtracting the Poiseuille flow profile (3.2) from the actual axial velocity.

At the end of the downstream rigid tube, the velocity profile is given by the (prescribed) Poiseuille profile and the axial velocity perturbation is therefore identically equal to zero. In the collapsible section, the wall motion induces noticeable perturbations to the mean Poiseuille flow, but the perturbations decay very rapidly in the upstream and downstream rigid tubes. The plots of the axial velocity perturbation confirm the two-layer structure predicted by the asymptotic analysis. The flow has an (inviscid) core region in which the velocities vary over $O(1)$ length scales; this region is surrounded by a thin Stokes layer of thickness $O(1/\alpha)$ near the wall. Furthermore, although the axial velocity perturbations can be of considerable size, their cross-sectional average is small as the positive and negative perturbations nearly cancel each other out, as predicted by (3.47). As a result, the wall motion generates only very small axial fluxes and the axial velocity perturbations at the inflow are negligible.

Figure 4 shows a more detailed comparison between the asymptotic (figure 4*a*) and numerical (figure 4*b*) results at $t = 0.05$. The plots of the transverse flows (instantaneous streamlines and pressure contours in the cross-section $z = 3$, shown

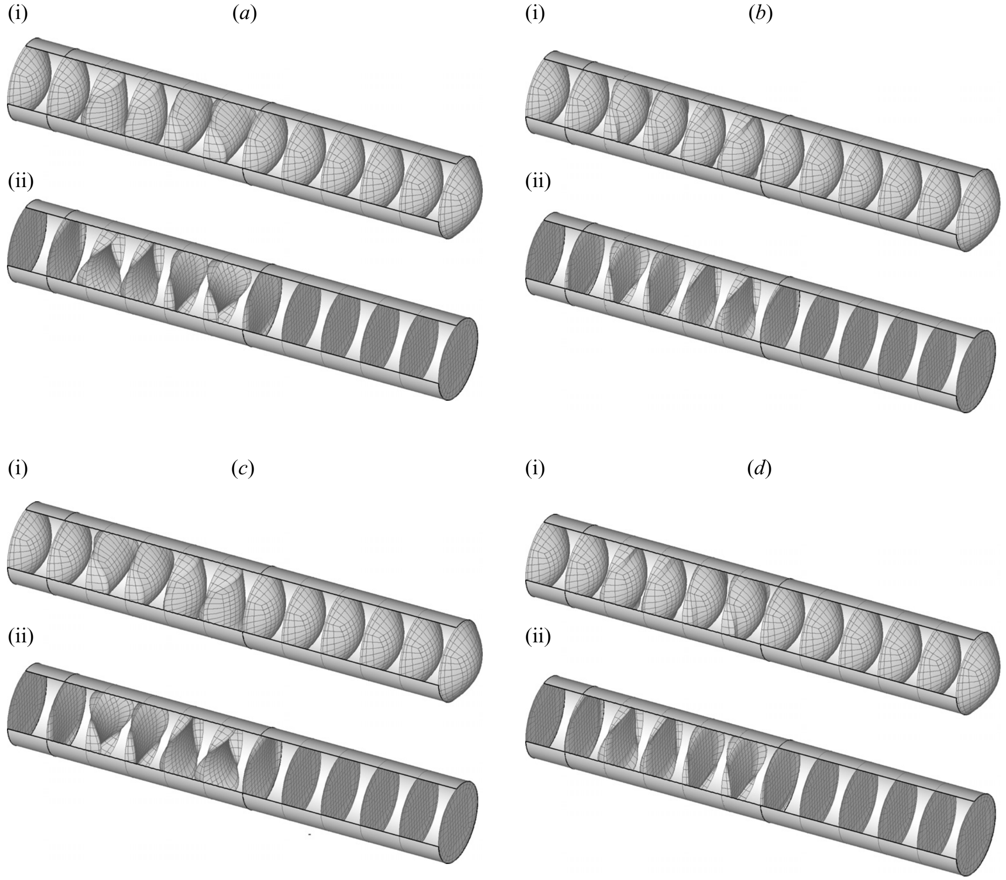

FIGURE 3. Profiles of the axial velocity, w, (i) and the axial velocity perturbation, $w - St^{-1}\overline{W}$, (ii) at (*a*) $t = 0.05$, (*b*) $t = 0.3$, (*c*) $t = 0.55$, (*d*) $t = 0.8$ for $\epsilon = 10^{-3}$, $St^{-1} = 10^{-3}$, $\mathscr{E} = 1$ and $\alpha^2 = 50$.

in (i)) demonstrate that the structure of these flows is identical to those analysed in Heil & Waters's (2006) study of two-dimensional flows in oscillating elastic rings. The transverse flows have an (inviscid) core region in which the velocity field resembles an unsteady stagnation point flow, surrounded by thin Stokes layers near the wall. The plots in (ii) demonstrate excellent agreement between the numerical and asymptotic predictions for the axial velocity profiles. Finally, the plots in (iii) show the three-dimensional pressure distribution $p(x, y, z)$, plotted as a function of the axial coordinate, z. The envelopes of these pressure plots indicate the maximum and minimum pressures in a given cross-section and therefore show that the pressure distribution in the rigid upstream and downstream tubes is dominated by the axial pressure gradient induced by the mean Poiseuille flow. Conversely, the pressure distribution in the collapsible segment is dominated by the pressure variations associated with the transverse flows. For instance, at $z = 3$, the pressure within the cross-section varies between $p_{min} = -0.259$ and $p_{max} = 0.212$, consistent with the range of pressures shown in the contour plots in (i).

An examination of the various terms in the energy equation (2.14), shown in figure 5, demonstrates that the system's energy budget is dominated by a balance between the (reversible) instantaneous rate-of-change of kinetic energy, $\mathrm{d}\Pi_{kin}/\mathrm{d}t$, and the rate-of-work done by the wall, $\mathscr{P}_{wall}$. Viscous dissipation continuously extracts

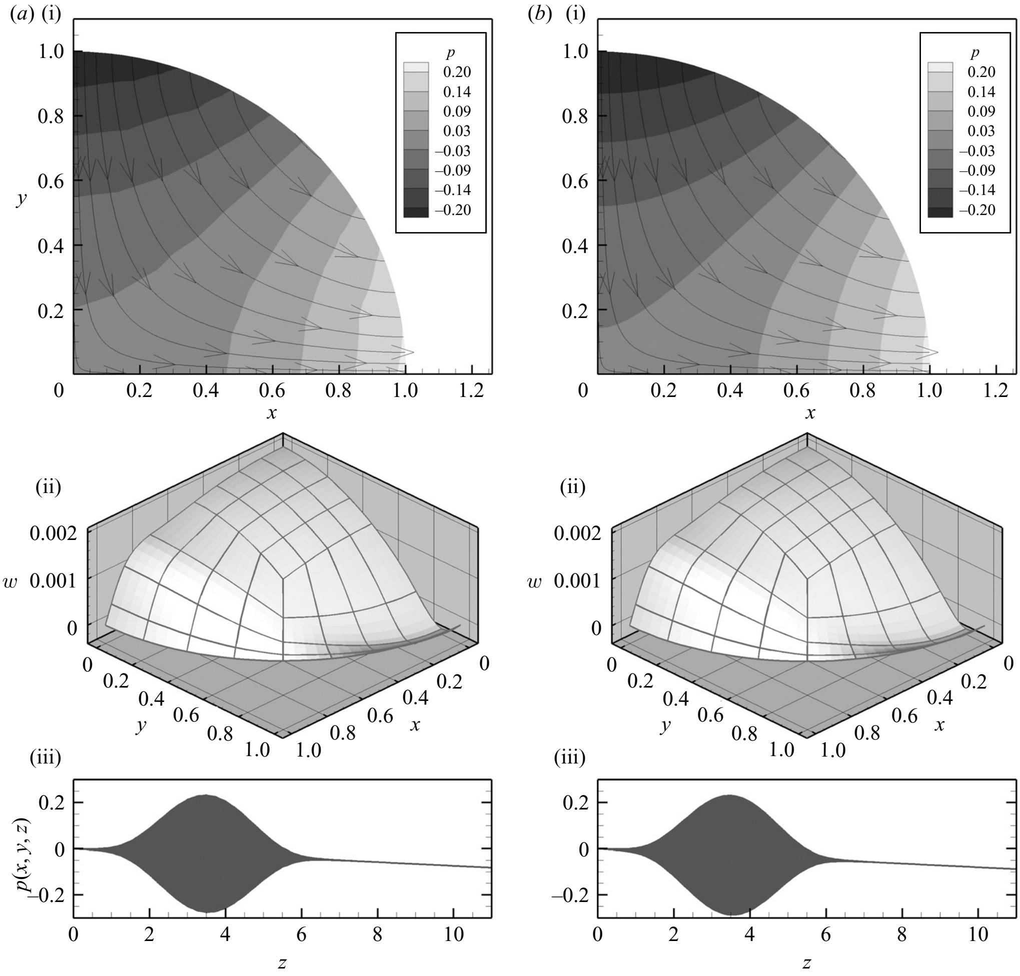

FIGURE 4. Comparison between (*a*) asymptotic and (*b*) numerical solutions for the flow field at $t = 0.05$ for $\epsilon = 10^{-3}$, $St^{-1} = 10^{-3}$, $\mathscr{E} = 1$ and $\alpha^2 = 50$. (i) Pressure contours and instantaneous streamlines in the cross-section $z = 3$. (ii) the axial velocity profile in the same cross-section. (iii) the three-dimensional pressure distribution $p(x, y, z)$ plotted as a function of the axial coordinate z.

energy from the system, while the net influx of kinetic energy and the rate-of-work done by the traction acting on the fluid at the in- and outflow cross-sections are very small. The wall therefore tends to extract energy from (or input energy into) the flow when its motion decelerates (or accelerates) the fluid. However, on average, the wall performs work on the fluid, as shown in figure 6 where we have plotted the total work done by the wall on the fluid,

$$\mathscr{W}_{wall}(t) = \int_0^t \mathscr{P}_{wall}(\tau)\,\mathrm{d}\tau, \tag{4.3}$$

as a function of time.

This indicates that the net axial sloshing flows generated by the wall motion are too small to allow Jensen & Heil's instability mechanism to generate a sufficiently large influx of kinetic energy to overcome the viscous dissipation. In a fluid–structure interaction problem we would therefore expect the wall motion to decay.

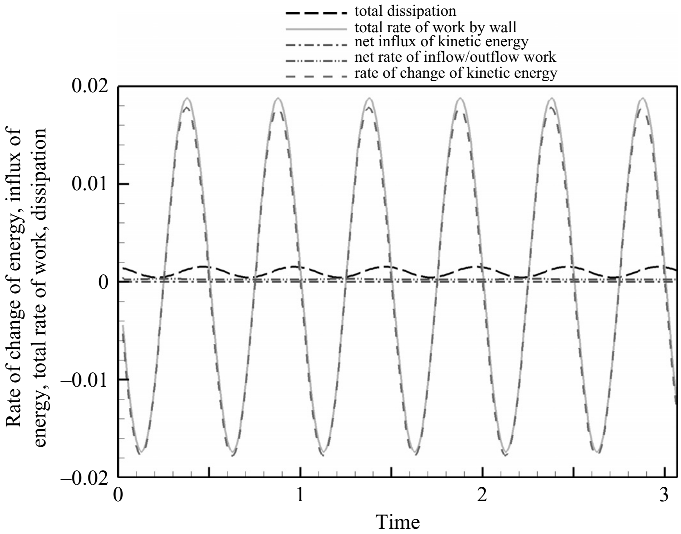

FIGURE 5. Analysis of the energy budget for the computations shown in figure 3. Time history of the various terms in the energy equation (2.14): total dissipation, $\mathscr{D}$; total rate of work by wall, $\mathscr{P}_{wall}$; net influx of kinetic energy, $\mathscr{F}_{in}^{[kin]} - \mathscr{F}_{out}^{[kin]}$; net rate-of-work at the inflow/outflow, $\mathscr{P}_{in} + \mathscr{P}_{out}$; rate of change of kinetic energy, $\mathrm{d}\Pi_{kin}/\mathrm{d}t$.

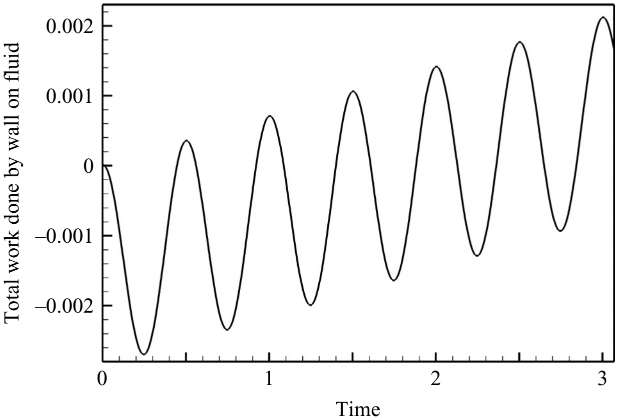

FIGURE 6. Evolution of the total work done by the wall on the fluid, $\mathscr{W}_{wall}(t)$, for the same parameters as in figures 3 and 5.

4.2. *Large-amplitude oscillations*

The introductory discussion in § 1 suggested that the instability mechanism proposed by Jensen & Heil (2003) should operate more efficiently for larger mean flows and/or for finite-amplitude wall oscillations. Therefore, we will now consider the system's behaviour for the same parameter values as in the previous section, but for a larger mean flow ($St^{-1} = 0.5$) and a wall motion in which the wall performs periodic oscillations of amplitude $\epsilon = 0.1$ about a buckled mean configuration ($\mathscr{E} = 1$).

Figure 7 shows the axial velocity profiles (the full profiles and the profiles of the axial velocity perturbation) in various cross-sections, while figure 8 shows the corresponding

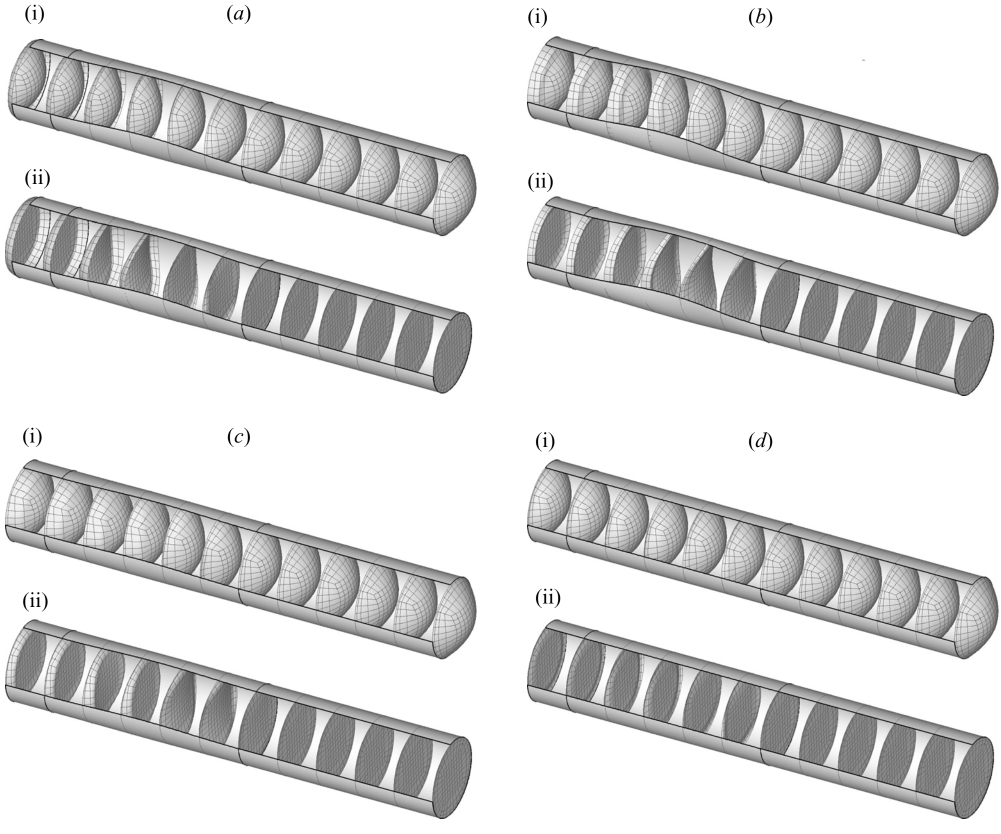

FIGURE 7. Profiles of the axial velocity, w, (i), the axial velocity perturbations, $w - St^{-1}\overline{W}$, (ii) at (*a*) $t=0.05$, (*b*) $t=0.3$, (*c*) $t=0.55$, (*d*) $t=0.8$ for $\epsilon=0.1$, $St^{-1}=0.5$, $\mathscr{E}=1$ and $\alpha^2=50$.

pressure distribution along the tube, at the same phases of the oscillation as in figure 3. As before, the axial velocity perturbation vanishes at the outflow, and the velocity perturbations generated within the collapsible segment decay very rapidly as the flow enters the downstream rigid tube. However, the large-amplitude wall motion now induces significant changes in the tube volume which generates large net axial sloshing flows in the upstream rigid tube. While these sloshing flows are not captured by the small-amplitude asymptotic analysis presented in §3, the character of the velocity perturbation is still consistent with the flow structures predicted there: an inviscid core region with thin Stokes layers near the boundary. Upon entering the upstream rigid section, the axial velocity perturbation rapidly approaches the classical Womersley profile with its characteristic flat velocity profile in the core region.

The (high-frequency) sloshing flows also have a major effect on the pressure distribution along the tube (figure 8). The inflow boundary conditions (2.10) impose a zero pressure at $z=0$. Since the core flow is dominated by a balance between unsteady inertia and the axial pressure gradient, $\partial \boldsymbol{u}/\partial t \approx -\nabla p$, see (3.14), the high-frequency sloshing motion of the fluid in the upstream rigid tube generates a large, predominantly axial, pressure gradient. The magnitude of the sloshing flow (and hence that of the induced axial pressure gradient) diminishes as we proceed downstream along the collapsible segment, within which the transverse flows can build up significant transverse pressure gradients. There are no (net) sloshing flows

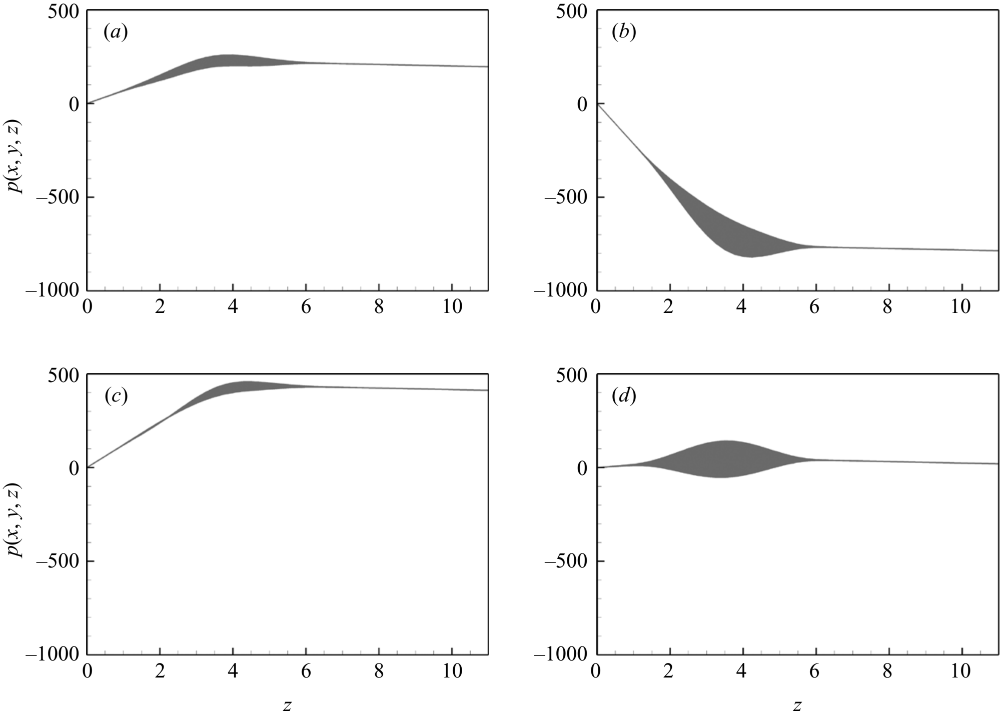

FIGURE 8. Pressure distribution along the tube at (*a*) $t = 0.05$, (*b*) $t = 0.3$, (*c*) $t = 0.55$, (*d*) $t = 0.8$. Parameter values as in figure 7.

in the downstream rigid tube, therefore the pressure distribution in this part of the system is dominated by the relatively small axial pressure gradient induced by the steady mean flow.

Figure 9 illustrates how the changes to the flow field affect the system's energy budget. For large-amplitude oscillations, the dominant terms in the energy equation are the rate-of-change of the kinetic energy, $\mathrm{d}\Pi_{kin}/\mathrm{d}t$, and $\mathscr{P}_{out}$, the rate-of-work done by the traction that acts on the fluid at the outflow. The latter arises through the product of the large pressure fluctuations at the outflow (figure 8), and the prescribed Poiseuille velocity profile. $\mathscr{P}_{out}$ represents the rate-of-work that a volumetric pump at the downstream end would have to provide in order to maintain a constant flow rate during the oscillations.

The sloshing flows generated in the upstream rigid tube now create a significant influx of kinetic energy. However, the influx of energy is still less than the viscous dissipation and, on average, the wall still performs work on the fluid.

A further increase in the influx of kinetic energy is therefore required to allow Jensen & Heil's instability mechanism to operate efficiently. Figure 10 shows the effect of an increase in the mean flow via an increase in the inverse Strouhal number St^{-1}. As the mean flow is increased, the wall performs less and less work on the fluid and for a sufficiently large value of St^{-1} the wall finally begins to extract energy from the flow. This suggests that in a fluid–structure interaction problem, the amplitude of the wall motion would increase, allowing the development of sustained self-excited oscillations of finite amplitude.

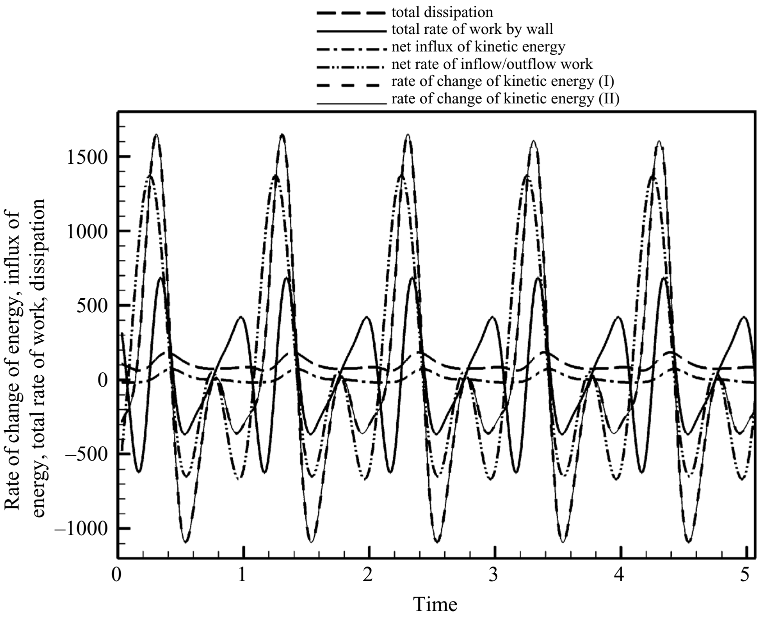

FIGURE 9. Analysis of the energy budget for the computations shown in figure 7: time history of the various terms in the energy equation (2.14). Total dissipation, $\mathscr{D}$; Total rate of work by wall, $\mathscr{P}_{wall}$; net influx of kinetic energy, $\mathscr{F}^{[kin]}_{in} - \mathscr{F}^{[kin]}_{out}$; net rate-of-work at the inflow/outflow, $\mathscr{P}_{in} + \mathscr{P}_{out}$; rate of change of kinetic energy, $\mathrm{d}\Pi_{kin}/\mathrm{d}t$. See Appendix B for a discussion of the two lines representing the rate-of-change of kinetic energy.

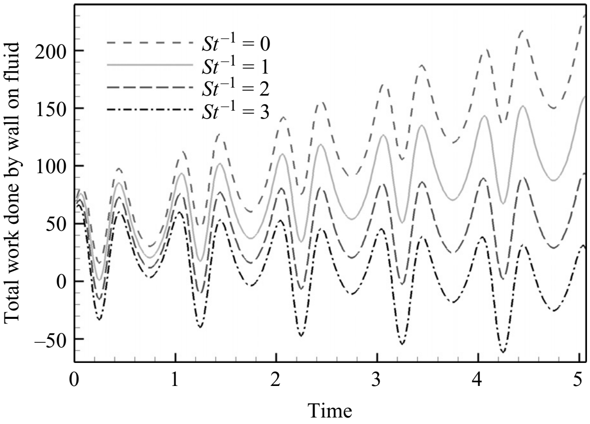

FIGURE 10. Evolution of the total work done by the wall on the fluid, $\mathscr{W}_{wall}(t)$, for $\alpha^2 = 50$ and a range of inverse Strouhal numbers. As the mean flow increases, the wall begins to extract energy from the flow. Other parameters as in figure 7.

5. Analysis of the energy budget

5.1. *The dependence of the rate-of-work done by the wall on St^{-1} and α^2*

To assess how the work done by the wall on the fluid varies with the mean flow, figure 11 shows a plot of the total work done by the wall over one period of the

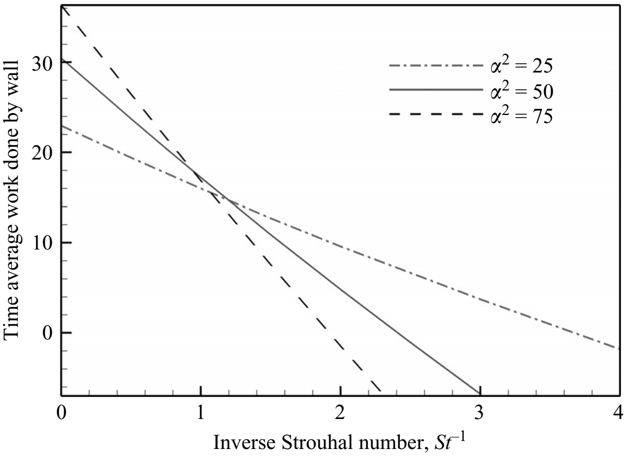

FIGURE 11. Work done by the wall on the fluid over one period of the oscillation, $\overline{\mathscr{P}_{wall}}$, as a function of the inverse Strouhal number for $\alpha^2 = 25,\ 50$ and 75. Other parameters as specified in figure 7.

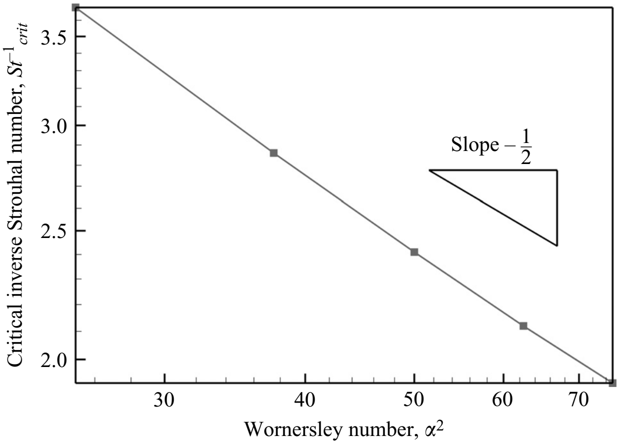

FIGURE 12. The critical Strouhal number at which the wall begins to extract energy from the flow as a function of the Womersley number α^2. Other parameters as specified in figure 7.

oscillation,

$$\overline{\mathscr{P}_{wall}} = \int_0^1 \mathscr{P}_{wall}(t)\,\mathrm{d}t, \tag{5.1}$$

as a function of the inverse Strouhal number. The figure shows that $\overline{\mathscr{P}_{wall}}$ decreases approximately linearly with St^{-1}. For $\alpha^2 = 50$ (the case considered in figure 10), $\overline{\mathscr{P}_{wall}}$ changes sign at $St^{-1} = St^{-1}_{crit} \approx 2.41$, implying that at this flow rate, the system performs energetically neutral oscillations without any net energy transfer between the fluid and the solid.

At larger Womersley numbers, the slope of the $\overline{\mathscr{P}_{wall}}(St^{-1})$ curves increases and the flow rate at which the wall begins to extract energy from the flow is reduced. This is analysed in more detail in figure 12 where we plot St^{-1}_{crit} as a function of the Womersley number, α^2, on a log–log scale. This plot may be interpreted as follows. Given the fluid properties, the tube diameter, and the frequency of the oscillation, i.e. given $\alpha^2 = \rho_f a^2/(\mu T)$, what is the minimum mean velocity U, expressed in terms of the inverse Strouhal number, $St^{-1} = UT/a$, required for the wall to extract energy from the flow?

The slope of the $St^{-1}_{crit}(\alpha^2)$ curve suggests that

$$St^{-1}_{crit} \sim \frac{1}{\alpha} \tag{5.2}$$

or, in dimensional terms

$$U_{crit} \sim \sqrt{\frac{\mu}{\rho_f T}} = \sqrt{\frac{\nu}{T}}, \tag{5.3}$$

which corresponds to a critical Reynolds number of

$$Re_{crit} = \frac{aU_{crit}}{\nu} \sim \alpha. \tag{5.4}$$

Thus, within the parameter regime considered here, lower-frequency oscillations require smaller mean flows in order for the wall to extract energy from the flow.

5.2. *A scaling argument to explain the dependence of St^{-1}_{crit} on α^2*

We shall now present simple scaling arguments to explain the relation (5.2) between the inverse Strouhal number St^{-1}_{crit} at which the oscillating tube wall begins to extract energy from the flow, and the Womersley number, α^2.

For this purpose, we note that for the boundary conditions chosen in this study, the time-averaged energy equation reduces to

$$\overline{\mathscr{P}_{wall}} = \overline{\mathscr{D}} - \overline{\mathscr{F}^{[kin]}_{in}} + \overline{\mathscr{F}^{[kin]}_{out}} - \overline{\mathscr{P}_{out}}. \tag{5.5}$$

The remaining terms in the energy equation (2.14) vanish: $\mathscr{P}_{in} \equiv 0$ because of the zero axial traction at the inflow; the time-average of the rate-of-change of kinetic energy vanishes because the system performs time-periodic oscillations. Furthermore, we recall that the flow in a collapsible tube that performs high-frequency oscillations of amplitude ϵ about a buckled mean configuration can be approximated by

$$\boldsymbol{u} = \frac{1}{St}\overline{W}\,\boldsymbol{e}_z + \epsilon\widehat{\boldsymbol{u}}_0 + \cdots, \quad p = -\frac{1}{St}8z + \epsilon\alpha^2\widehat{p}_0 + \cdots, \tag{5.6}$$

where the time-periodic perturbations $\widehat{\boldsymbol{u}}_0$ and $\widehat{p}_0$ have zero mean and the unsteady oscillatory flow $\widehat{\boldsymbol{u}}_0$ has an inviscid core with thin Stokes layers of thickness $\delta = O(1/\alpha)$ near the tube walls. (We note that, for small-amplitude high-frequency oscillations, it is possible to provide rigorous bounds on the terms that are neglected in the following estimates. However, in the interest of brevity we shall present only the estimates for the leading-order terms and represent the remaining smaller terms by '. . .'.)

5.2.1. *Net influx of kinetic energy*

The time-averaged net influx of kinetic energy, $\overline{\mathscr{F}^{[kin]}_{net}}$, is given by $\overline{\mathscr{F}^{[kin]}_{in}} - \overline{\mathscr{F}^{[kin]}_{out}}$. Inserting (5.6) into the definition of $\mathscr{F}^{[kin]}_{in/out}(t)$ in (2.14) and taking the time-average yields

$$\overline{\mathscr{F}^{[kin]}_{net}} = \alpha^2\left[\int \frac{1}{St^3}\left(\tfrac{1}{2}\overline{W^3}\right)\mathrm{d}A + \int \frac{\epsilon^2}{St}\left(\tfrac{1}{2}\overline{W}\,\overline{\widehat{w}_0^2}\right)\mathrm{d}A + \cdots\right]\Bigg|_{z=L_{total}}^{z=0}. \tag{5.7}$$

When adding the contributions from the in- and outflow cross-sections, the flux of kinetic energy associated with the mean flow, represented by the first integral in this expression, cancels; the second term vanishes at the outflow where $\widehat{w}_0 = 0$. Therefore we obtain the estimate

$$\overline{\mathscr{F}^{[kin]}_{net}} = O\left(\epsilon^2 \frac{\alpha^2}{St}\right) + \cdots. \tag{5.8}$$

5.2.2. *Work done on the fluid at the outflow*

Since Poiseuille flow, $St^{-1}\overline{W}(r)\boldsymbol{e}_z$ is imposed at the outflow, the instantaneous rate of work on the fluid at the outflow is given by

$$\mathscr{P}_{out}(t) = -\int \frac{1}{St}\overline{W}\; p|_{z=L_{total}}\, \mathrm{d}A. \tag{5.9}$$

Substituting (5.6) and taking the time-average then yields

$$\overline{\mathscr{P}_{out}} = \mathscr{P}^{[Pois]}_{out} + O\left(\frac{\epsilon^2\alpha^2}{St}\right) + \cdots, \tag{5.10}$$

where

$$\mathscr{P}^{[Pois]}_{out} = \int \frac{8}{St^2}\overline{W}\; L_{total}\, \mathrm{d}A \tag{5.11}$$

is the rate of work required to drive the steady mean flow through the undeformed, axisymmetric tube, and the $O(\epsilon^2\alpha^2/St)$ contribution arises from the work done by the Reynolds-stress-induced pressure at the outflow.

5.2.3. *Viscous dissipation*

Finally, we estimate the time-averaged viscous dissipation. The expression for dissipation involves integration over a time-varying volume. We exploit the assumption $\epsilon \ll 1$ to approximate the integral over the time-dependent volume with an integral over the volume of the mean configuration of the tube. The time-mean dissipation is given by $\overline{\Phi} = 2\ \overline{\boldsymbol{E}:\boldsymbol{E}} = 2\ \overline{\boldsymbol{E}}:\overline{\boldsymbol{E}} + 2\ \overline{\widehat{\boldsymbol{E}}:\widehat{\boldsymbol{E}}}$. From (5.6), we find that the dominant contribution to $\overline{\boldsymbol{E}}$ comes from the Poiseuille flow, and it is straightforward to show that the resulting contribution to the dissipation is $\mathscr{P}^{[Pois]}_{out}$. The dominant contribution to $\widehat{\boldsymbol{E}}$ arises from the velocity gradients in the Stokes-layer within which the velocity varies by $O(\epsilon)$ over the Stokes-layer thickness $\delta = O(1/\alpha)$. Hence, $\widehat{\boldsymbol{E}} = O(\alpha\epsilon)$ and the integral of $\overline{\widehat{\boldsymbol{E}}:\widehat{\boldsymbol{E}}}$ over the Stokes layer gives a contribution of $O(\epsilon^2\alpha)$ so that

$$\overline{\mathscr{D}} = \mathscr{P}^{[Pois]}_{out} + O(\epsilon^2\alpha) + \cdots. \tag{5.12}$$

5.2.4. *Rate of work done by the wall on the fluid*

Upon inserting the estimates (5.8), (5.10) and (5.12) into (5.5), $\mathscr{P}^{[Pois]}_{out}$ in (5.10) cancels with the viscous dissipation associated with the mean flow in (5.12). Hence, an order-of-magnitude estimate for the time-average work done by the wall on the fluid is given by

$$\overline{\mathscr{P}_{wall}} \approx O(\epsilon^2\alpha) - O\left(\epsilon^2\frac{\alpha^2}{St}\right), \tag{5.13}$$

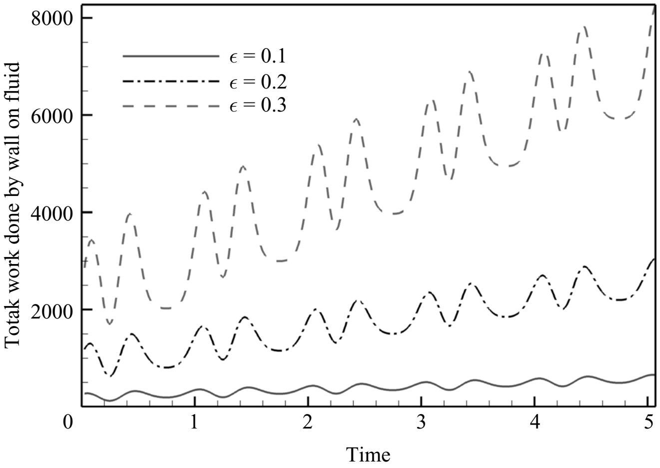

FIGURE 13. Evolution of the total work done by the wall on the fluid, $\mathscr{W}_{wall}(t)$, for a mean deflection of $\epsilon\mathscr{E} = 0.3$ and various different amplitudes of the oscillation. $St^{-1} = 1,\ \alpha^2 = 25$.

which shows that the sign of the work done by the wall on the fluid changes when $\alpha \sim \alpha^2/St$, i.e.

$$St_{crit}^{-1} \sim \frac{1}{\alpha}, \tag{5.14}$$

which is consistent with the numerical results shown in figure 12.

5.3. *The dependence of the energy budget on the mean and oscillatory amplitudes of the wall motion*

Within the framework of the instability mechanism considered here, the dominant source of energy is the influx of kinetic energy over the inflow boundary. We discussed in §1 that the influx of kinetic energy may be increased by increasing the amplitude of the sloshing flows and/or by increasing the mean flow. The estimate (5.13) shows that an increase in mean flow (via an increase in St^{-1}) will always reduce the work done by the wall on the fluid. The magnitude of the sloshing flows may be increased by increasing the amplitude of the wall oscillation. However, this also affects the viscous dissipation in the Stokes layers, and the estimate (5.13) shows that the viscous dissipation and the net influx of kinetic energy have the same dependence on the amplitude of the oscillations. Therefore an increase in ϵ will not change the sign of the net work done by the wall on the fluid. This is confirmed by our numerical simulations. As an example, figure 13 shows the total work done by the wall on the fluid, $\mathscr{W}_{wall}(t)$, for a wall that performs oscillations of various amplitudes ϵ, about a mean displacement of amplitude $\epsilon\mathscr{E} = 0.3$. The increase in ϵ strongly increases the magnitude of the sloshing flows, but the wall continues to do net work on the fluid for all values of ϵ.

The scaling argument presented in the previous section assumes that wall displacements of amplitude ϵ generate $O(\epsilon)$ axial sloshing flows. We stressed in §1 that in three-dimensions, this is true only if the tube wall performs oscillations about a non-axisymmetrically buckled mean configuration and consequently set $\mathscr{E} \neq 0$ in all the computations presented so far. Figure 14 demonstrates that the behaviour of flows in collapsible tubes that perform oscillations about an axisymmetric mean configuration does indeed differ significantly from the behaviour reported earlier. While an increase in the mean flow still reduces the average work done by the wall on

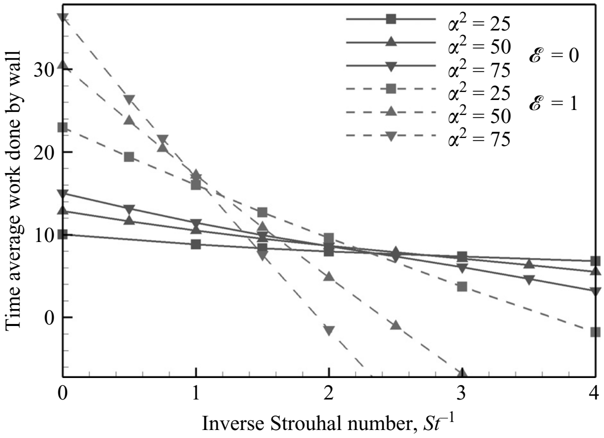

FIGURE 14. Work done by the wall on the fluid over one period of the oscillation, $\overline{\mathscr{P}_{wall}}$, for oscillations of amplitude $\epsilon = 0.1$ about an axisymmetric ($\mathscr{E} = 0$) or non-axisymmetric ($\mathscr{E} = 1$) mean configuration.

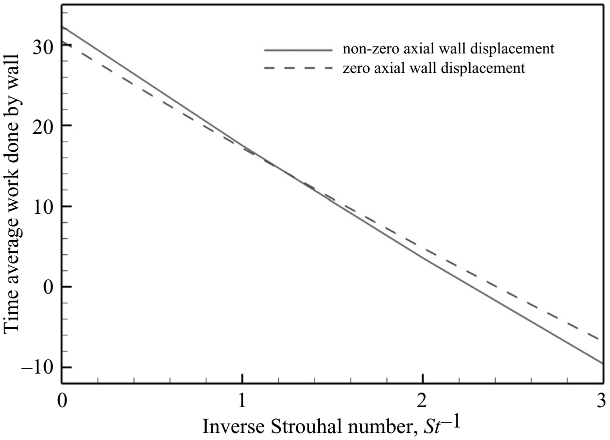

FIGURE 15. Work done by the wall on the fluid over one period of the oscillation, $\overline{\mathscr{P}_{wall}}$, for wall oscillations with different mode shapes. Dashed line, zero axial displacements ($\mathbb{B} = 0$). Solid line, non-zero axial displacements ($\mathbb{B} = 0.1$). $\alpha^2 = 50$, $\epsilon = 0.1$ and $\mathscr{E} = 1$.

the fluid, the decay is much more gradual and, within the range of inverse Strouhal numbers considered, the wall never extracts energy from the flow, indicating that Jensen & Heil's instability mechanism is too weak to allow the onset of self-excited oscillations. This is consistent with Bertram's experimental observations (personal communication, 2007).

5.4. *Variations in the (prescribed) wall displacement field*

The analysis presented in this paper requires the specification of the wall displacement field. To demonstrate that the details of the wall deformation do not strongly affect the results, figure 15 shows a plot of the work done by the wall over one period of the oscillation, $\overline{\mathscr{P}_{wall}}$, as a function of the inverse Strouhal number for two different mode shapes. The solid line represents the data obtained in our previous computations in which the axial wall displacement was suppressed by setting $\mathscr{W}(\xi^1) = 0$; the dashed line was obtained from a second series of computations in which the wall motion included a significant axial component which induced a strong warping of the cross-sections. This was achieved by setting

$$\mathscr{W}(\xi^1) = \begin{cases} 0 & \text{for } \xi^1 < L_{up}, \\ \mathbb{B} \sin\left(\dfrac{2\pi(\xi^1 - L_{up})}{L}\right) & \text{for } L_{up} < \xi^1 < L_{up} + L, \\ 0 & \text{for } \xi^1 > L + L_{up}. \end{cases} \tag{5.15}$$

Even though the large axial wall velocities created by this wall displacement field strongly affect the flow inside the Stokes layers, the system's qualitative behaviour remains unchanged. In particular, an increase in the mean flow still leads to a proportional reduction in the work done by the wall on the fluid, and there exists a critical value of St^{-1} above which the wall begins to extract energy from the flow.

6. Discussion

We have studied finite-Reynolds-number flows in three-dimensional collapsible tubes whose walls perform (prescribed) high-frequency oscillations of finite amplitude. The analysis of the system's energy budget allowed us to identify conditions under which the wall extracts energy from the mean flow. In the parameter regime considered here, the main source of energy was shown to be the influx of kinetic energy generated by the axial sloshing flows that are driven by the oscillatory wall motion; the wall extracts energy from the flow if the net influx of kinetic energy exceeds the viscous dissipation in the flow.

In a fully coupled fluid–structure interaction problem in which the wall motion is not prescribed, any energy extracted from the flow will be transferred to the wall's strain and kinetic energies, and therefore lead to an increase in the amplitude of the wall motion. Wall motions for which there is no net transfer of energy between the fluid and the wall therefore correspond to sustained self-excited oscillations whereas the wall oscillation would be expected to decay if the fluid continuously extracts energy from the wall.

Since wall oscillations about an axisymmetric mean configuration create only very weak sloshing flows and therefore generate only a small net influx of kinetic energy, our analysis predicts that self-excited oscillations will develop much more readily from a non-axisymmetrically buckled rather than an axisymmetric mean configuration, which is in pleasing agreement with the experimental observations of Bertram (personal communication, 2007).

The analysis presented in this paper was performed with a prescribed wall motion whereas in a fully coupled fluid–structure interaction problem the mode shape and the period of the wall oscillation would have to be determined from the coupled solution of the fluid and solid equations. We have already demonstrated in § 5.4 that our results are not particularly sensitive to variations in the mode shape. So far we have not made any assumptions about the mechanism that controls the period $\mathscr{T}$ of the fully coupled oscillations. If we assume that the oscillations are governed by a dynamic balance between unsteady fluid inertia (with pressures of size $O(\rho_f(a/\mathscr{T})^2)$) and the wall stiffness (characterized, e.g. by the tube's bending stiffness, K) and thus require that

$$\rho_f \left(\frac{a}{\mathscr{T}}\right)^2 \sim K, \tag{6.1}$$

we obtain an estimate for the period of the oscillation as

$$\mathscr{T} \sim a\sqrt{\frac{\rho_f}{K}}. \tag{6.2}$$

We note that this estimate was found to be very accurate in Heil & Waters's (2006) study of the oscillation of fluid-filled elastic rings. The frequency of the oscillations is therefore determined by the system's material properties, and high-frequency oscillations may be realized by making the tube wall sufficiently stiff. Furthermore, using $T = a\sqrt{\rho_f/K}$ to non-dimensionalize time shows that

$$\alpha^2 = \frac{a}{\mu}\sqrt{K\rho_f}, \tag{6.3}$$

indicating that the Womersley number of the flow (and, by virtue of (5.4), the critical Reynolds number beyond which self-excited oscillations are likely to develop) depends only on the system's material properties.

Our analysis showed that in a given experiment (constant fluid properties and tube dimensions) and a fixed frequency of the oscillation (i.e. fixed Womersley number α^2), self-excited oscillations are likely to develop when the mean flow (expressed in terms of the inverse Strouhal number, St^{-1}) exceeds a certain threshold, St_{crit}^{-1}. We note that since $Re = \alpha^2/St$, an increase in St^{-1} at fixed α^2 corresponds to an increase in the Reynolds number associated with the mean flow. The observation that self-excited oscillations are likely to develop when $St^{-1} > St_{crit}^{-1}$ is therefore consistent with the experimental observation that collapsible tube oscillations develop only at sufficiently large Reynolds number. While this is consistent with the behaviour observed in most fluid mechanical instabilities, we wish to stress that the mechanism for the onset of self-excited oscillations presented in this study does not rely on a fluid-mechanical instability, but involves a genuine interaction between fluid and solid mechanics: small-amplitude wall oscillations generate axial sloshing flows; the sloshing flows generate a net influx of kinetic energy into the system; the excess energy is extracted by the wall and leads to an increase in the amplitude of the oscillation.

Finally, we assess how our predictions for the minimum velocity required for the onset of self-excited oscillations compares to the predictions from the one-dimensional models discussed in § 1. Assuming that the tube law, $\mathfrak{P}(A^*)$, scales with the tube's bending stiffness, K, the assumption that self-excited oscillations develop when the fluid velocity reaches the wave speed c, given by (1.1), yields

$$U_{crit} \sim \sqrt{\frac{K}{\rho_f}}, \tag{6.4}$$

whereas our estimate (5.3), together with (6.3) yields

$$U_{crit} \sim \sqrt{\frac{\nu}{a}\sqrt{\frac{K}{\rho_f}}}, \tag{6.5}$$

indicating that the two mechanisms operate in different parameter regimes.

The authors wish to acknowledge many helpful discussions with Chris Bertram, Andrew Hazel, Oliver Jensen and Robert Whittaker. The numerical simulations benefited greatly from Jonathan Boyle's work on the development of Navier–Stokes

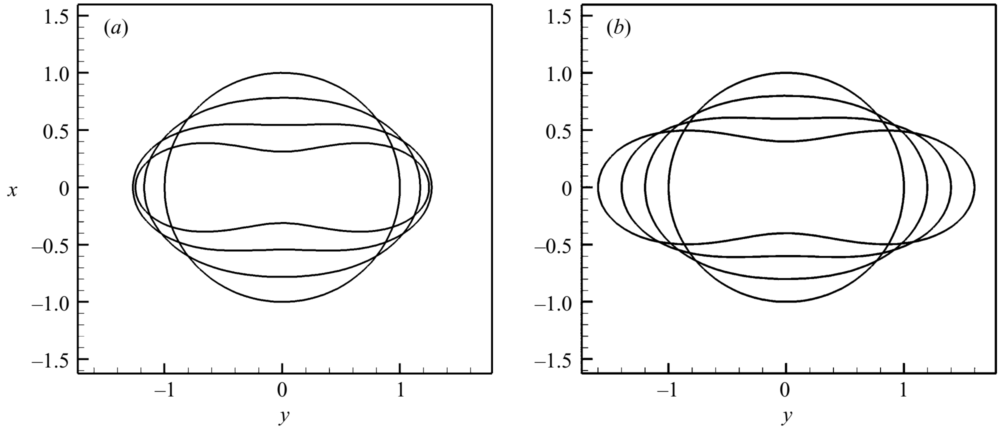

FIGURE 16. Plot showing the deformation of the tube's cross-sections with (*a*) and without (*b*) the normalizing factor $\mathscr{S}(t,\xi^1;\epsilon)$ which suppresses the net azimuthal extension of the tube wall.

preconditioners in oomph-lib. The research was supported by a grant from EPSRC and an EPSRC Advanced Research Fellowship for S. L. W.

Appendix A. The modification of the wall displacement field for large-amplitude deformations

For small-amplitude oscillations, the eigenmodes of freely oscillating elastic rings, modulated by the axial mode shape specified in (4.1), generate plausible wall deformations. However, as the amplitude of the oscillation increases, this simple wall displacement field introduces significant azimuthal stretching of the tube wall, as illustrated in figure 16. This creates unrealistic deformations since thin-walled elastic tubes tend to deform such that their extensional deformation is minimized.

To correct this, we defined the scaling factor $\mathscr{S}(t,\xi^1;\epsilon)$ in (2.4) as

$$\mathscr{S}(t,\xi^1;\epsilon) = 2\pi\left(\int_0^{2\pi}\left|\frac{\partial\widetilde{\boldsymbol{R}_w^{\perp}}(\xi^1,\xi^2,t;\epsilon)}{\partial\xi^2}\right|\mathrm{d}\xi^2\right)^{-1}. \tag{A 1}$$

The modification ensures that the tube wall deforms without any net azimuthal extension. In the computations with the specific wall shape described in §4 we employed the approximation $\mathscr{S}(t,\xi^1;\epsilon) = 1 - 0.555d^2 - 0.177d^4 + 0.053d^6$ where $d = \mathscr{U}(\xi^1)f(t)$ is the instantaneous amplitude of the radial wall displacement in the cross-section $z = \xi^1$. This results in much more realistic deformations, as illustrated in figure 16(*b*). In particular, without the normalization, the material points that initially buckled outwards continue to move outwards as the amplitude of the deflection increases. With the normalization, these points move back towards the centre when the cross-section approaches an '∞'-shape, as observed in actual collapsible tubes. We note that for $\mathscr{E} = 0$ we have $\mathscr{S}(t,\xi^1;\epsilon) = 1 + O(\epsilon^2)$, therefore the modification to the wall displacement field does not change its behaviour for small deflections. Specifically, we retain the important property that for oscillations about the axisymmetric state the change in tube volume is a second-order effect in terms of the displacement amplitude, ϵ.

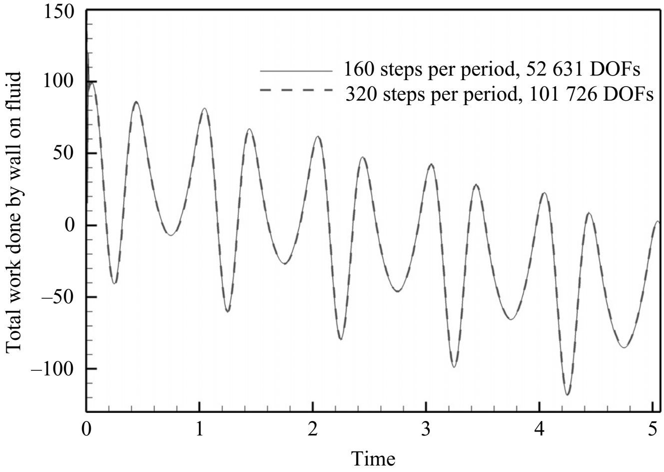

FIGURE 17. Convergence test showing the time history of the total work done by the wall, $\mathscr{W}_{wall}(t)$, computed with our standard resolution involving approximately 52 600 DOFs and 160 time steps per period, and the same data computed on a finer mesh with approximately 101 700 DOFs and with 320 time steps per period. $St^{-1}=3$, $\alpha^2=75$, $\epsilon=0.1$ and $\mathscr{E}=1$.

Appendix B. Convergence tests

In addition to the detailed comparison between the asymptotic and numerical results for small-amplitude oscillations, presented in §4.1, we performed a number of additional tests to assess the accuracy of our computations. Figure 17 shows the results of a convergence test, performed to document the mesh and time-step independence of the numerical results for finite-amplitude oscillations with $\epsilon=0.1$ and $\mathscr{E}=1$. The plot compares the evolution of the total work done by the wall on the fluid – the key quantity used in the analysis of the system's energy budget – computed with our standard resolution (approximately 52 600 degrees of freedom (DOFs) and 160 time steps per period), against the results obtained on a finer mesh with approximately 101 700 DOFs and with 320 time steps per period. Both computations were performed for the parameters $St^{-1}=3$ and $\alpha^2=75$, resulting in the largest Reynolds and Womersley numbers used in any of the simulations presented in this paper.

Further consistency checks for the numerical results are contained in the plot of the energy budget in figure 9 where the rate-of-change of kinetic energy, $\mathrm{d}\Pi_{kin}/\mathrm{d}t$, is plotted twice. Curve I was obtained by finite-differencing the instantaneous kinetic energy Π_{kin} which can be obtained directly from the computed velocity field; curve II was obtained by computing $\mathrm{d}\Pi_{kin}/\mathrm{d}t$ indirectly, by adding up the remaining quantities in the energy equation (2.14). Curves I and II are indistinguishable.

REFERENCES

BERTRAM, C. & TSCHERRY, J. 2006 The onset of flow-rate limitation and flow-induced oscillations in collapsible tubes. *J. Fluids Struct.* **22**, 1029–1045.

BERTRAM, C. D. & CASTLES, R. J. 1999 Flow limitation in uniform thick-walled collapsible tubes. *J. Fluids Struct.* **13**, 399–418.

BERTRAM, C. D. & RAYMOND, C. J. 1991 Measurements of wave speed and compliance in a collapsible tube during self-excited oscillations: a test of the choking hypothesis. *Med. Biol. Engng Comput.* **29**, 493–500.

Bertram, C. D., Raymond, C. J. & Pedley, T. J. 1990 Mapping of instabilities for flow through collapsible tubes of differering length. *J. Fluids Struct.* **4**, 125–153.

Elman, H. C., Silvester, D. J. & Wathen, A. J. 2005 *Finite Elements and Fast Iterative Solvers with Applications in Incompressible Fluid Dynamics*. Oxford University Press.

Heil, M. & Hazel, A. L. 2006 `oomph-lib` – an object-oriented multi-physics finite-element library. In *Fluid–Structure Interaction* (ed. M. Schäfer & H.-J. Bungartz), pp. 19–49. Springer. `oomph-lib` is available as open-source software at `http://www.oomph-lib.org`.

Heil, M. & Jensen, O. E. 2003 Flows in deformable tubes and channels – theoretical models and biological applications. In *Flow in Collapsible Tubes and Past Other Highly Compliant Boundaries* (ed. T. J. Pedley & P. W. Carpenter), pp. 15–50. Kluwer.

Heil, M. & Waters, S. 2006 Transverse flows in rapidly oscillating, elastic cylindrical shells. *J. Fluid Mech.* **547**, 185–214.

Hinch, E. J. 1991 *Perturbation Methods*. Cambridge University Press.

Jensen, O. E. & Heil, M. 2003 High-frequency self-excited oscillations in a collapsible-channel flow. *J. Fluid Mech.* **481**, 235–268.

Luo, X. Y. & Pedley, T. J. 2000 Multiple solutions and flow limitation in collapsible channel flows. *J. Fluid Mech.* **420**, 301–324.

Soedel, W. 1993 *Vibrations of Shells and Plates*. Marcel Dekker.

Van Dyke, M. 1964 *Perturbation Methods in Fluid Mechanics*. Academic.